


2016-01-01

Computational Modeling of a 60kW Oxy-Methane Direct Power Extraction Combustor

Omar Daniel Vidana

University of Texas at El Paso, odvidana@miners.utep.edu

Follow this and additional works at: https://digitalcommons.utep.edu/open_etd

 Part of the [Aerospace Engineering Commons](#), [Mechanical Engineering Commons](#), and the [Oil, Gas, and Energy Commons](#)

Recommended Citation

Vidana, Omar Daniel, "Computational Modeling of a 60kW Oxy-Methane Direct Power Extraction Combustor" (2016). *Open Access Theses & Dissertations*. 979.

https://digitalcommons.utep.edu/open_etd/979

This is brought to you for free and open access by DigitalCommons@UTEP. It has been accepted for inclusion in Open Access Theses & Dissertations by an authorized administrator of DigitalCommons@UTEP. For more information, please contact lweber@utep.edu.

COMPUTATIONAL MODELING OF A 60KW OXY-METHANE DIRECT
POWER EXTRACTION COMBUSTOR

OMAR DANIEL VIDAÑA

Master's Program in Mechanical Engineering

APPROVED:

Norman Love, Ph.D., Chair

Yirong Lin, Ph.D.

Bill Tseng, Ph.D.

Charles Amber, Ph.D.
Dean of the Graduate School

Copyright ©

by

Omar D. Vidaña

2016

Dedication

I dedicate this thesis to my mother. I'm here because of your support and sacrifices, gracias mama! Thanks also to Dr. Norman Love, for giving me the opportunity to acquire engineering experience that I will carry on for the rest of my life.

COMPUTATIONAL MODELING OF A 60KW OXY-METHANE DIRECT
POWER EXTRACTION COMBUSTOR

by

OMAR DANIEL VIDANA, B.S.M.E.

THESIS

Presented to the Faculty of the Graduate School of

The University of Texas at El Paso

in Partial Fulfillment

of the Requirements

for the Degree of

MASTER OF SCIENCE

Master's Program in Mechanical Engineering

THE UNIVERSITY OF TEXAS AT EL PASO

August, 2016

Acknowledgements

The research is supported by the US Department of Energy, under award DE-FE-0024062 (Project Manager Jason Hissam). However, any opinions, findings, conclusions, or recommendations expressed herein are those of the authors and do not necessarily reflect the views of the Department of Energy.

Table of Contents

| | |
|--|------|
| Acknowledgements | v |
| Table of Contents | vi |
| List of Tables | viii |
| List of Figures | ix |
| Chapter 1: Introduction and Background..... | 1 |
| 1.1 Overview | 1 |
| 1.2 Magnetohydrodynamic Power Generators | 2 |
| 1.3 Faraday’s Principle | 3 |
| 1.4 Previous Work | 4 |
| Chapter 2: Theory | 7 |
| 2.1 Fundamental Equations..... | 7 |
| 2.2 Mesh..... | 19 |
| 2.3 Boundary Conditions | 21 |
| Chapter 3: Results and Discussion..... | 25 |
| 3.1 Swirl Coaxial Injector | 25 |
| 3.2 Converging-Diverging Nozzle..... | 29 |
| 3.3 Cooling System | 36 |
| Chapter 4: Summary and Conclusions..... | 38 |
| References | 40 |
| Appendix A: Sample Calculations..... | 42 |
| Fuel & Oxidizer Mass Flow Rates | 42 |
| Throat Conditions | 43 |
| Cooling System Pump Optimal Flow Rate | 45 |
| CEA Results | 49 |
| Appendix B: CADs and Schematics | 51 |
| DPE Combustor Assembly | 51 |
| DPE Combustor Exploded View | 52 |
| DPE Combustor | 53 |

| | |
|---------------------------|----|
| Cooling Jacket..... | 54 |
| Fuel Manifold..... | 55 |
| Water Line Schematic..... | 56 |
| Vita | 57 |

List of Tables

| | |
|--|----|
| Table 1: Enthalpy Extraction Percentages | 5 |
| Table 2: Governing equations variables | 8 |
| Table 3: Injector pressure drop variables | 10 |
| Table 4: Non-premixed model variables | 13 |
| Table 5: Combined stress & Sieder-Tate equation variables | 16 |
| Table 6: Cooling system model variables | 18 |
| Table 7: Boundary conditions for the swirl coaxial injector | 22 |
| Table 8: Boundary conditions for the converging-diverging nozzle | 23 |
| Table 9: Boundary conditions for the cooling system | 24 |
| Table 10: Results comparison between CEA and Fluent model | 29 |
| Table 11: Flow rate calculation variables | 43 |
| Table 12: Heat flux calculation values | 44 |
| Table 13: Combined stress calculation values | 44 |
| Table 14: Components pressure drop | 45 |
| Table 15: Sudden expansion, sudden contraction and bends pressure drop | 46 |
| Table 16: Pressure drop along the pipes | 46 |
| Table 17: Head loss and ΔP at various flow rates | 47 |

List of Figures

| | |
|---|----|
| Figure 1: Turbogenerator vs. MHD generator | 2 |
| Figure 2: Gas conductivity vs. Ionization for open cycle MHD generators | 3 |
| Figure 3: Fleming's Right Hand Rule..... | 4 |
| Figure 4: DPE combustor drawing | 7 |
| Figure 5: Swirl coaxial injector..... | 9 |
| Figure 6: Early swirl coaxial injector with ring manifold..... | 11 |
| Figure 7: DPE combustor and converging-diverging nozzle..... | 12 |
| Figure 8: : Simplified DPE combustor..... | 14 |
| Figure 9: DPE combustor concept | 15 |
| Figure 10: Cooling channels | 16 |
| Figure 11: Cooling Jacket | 17 |
| Figure 12: Simplified cooling system model | 19 |
| Figure 13: Swirl coaxial injector mesh | 20 |
| Figure 14: Combustor and converging-diverging nozzle mesh..... | 20 |
| Figure 15: Cooling system mesh..... | 21 |
| Figure 16: Fuel injector static pressure controur, units shown are in kPa | 25 |
| Figure 17: Fuel injector velocity contour, units shown in m/s | 26 |
| Figure 18(a): Injector volume fraction contour of methane at 0.1 ms | 26 |
| Figure 18(b): Injector volume fraction contour of methane at 0.5 ms..... | 26 |
| Figure 18(c): Injector volume fraction contour of methane at 1 ms | 27 |
| Figure 18(d): Injector volume fraction contour of methane at 2 ms | 27 |
| Figure 18(e): Injector volume fraction contour of methane at 4.45 ms | 27 |
| Figure 19: Early fuel injector static pressure controur, units shown are in kPa | 28 |
| Figure 20: Early fuel injector velocity contour, units shown are in m/s..... | 28 |
| Figure 21: Early injector volume fraction contours of methane at 1 and 3 ms..... | 29 |
| Figure 22: Velocity contour with combustion, units shown are in m/s | 30 |
| Figure 23: Temperature contour with combustion, units shown are in K | 30 |
| Figure 24: Methane velocity vectors..... | 31 |
| Figure 25: Methane pathlines..... | 32 |
| Figure 26: Oxygen pathlines | 32 |
| Figure 27: Converging-diverging nozzle boundary layer | 33 |
| Figure 28: Simplified combustor velocity contour, units shown are in m/s | 34 |
| Figure 29: Simplified combustor temperature contour, units shown are in K..... | 34 |
| Figure 30: Simplified combustor methane velocity vectors | 35 |
| Figure 31: Simplified combustor methane pathlines | 35 |
| Figure 32: Simplified combustor oxygen pathlines | 36 |
| Figure 33: Temperature contour for the cooling system, units shown are in K..... | 37 |
| Figure 34: Simplified cooling system pressure contour | 37 |
| Figure 35: DPE combustor..... | 39 |
| Figure 36: Sudden contractions loss coefficient chart | 45 |
| Figure 37: Pump performance curve vs. System curve | 48 |

Chapter 1: Introduction and Background

1.1 OVERVIEW

Recently, the demand for alternative sources of energy has increased. This is partially due to the effects observed over many years of burning coal and other fossil fuels to generate electricity. The main disadvantage of burning coal and fossil fuels is the amount of carbon dioxide produced. Coal and fossil fuels were responsible for 31% of the 6,673 million metric tons of carbon dioxide emitted in United States in 2013¹. Although carbon dioxide is a primary pollutant, power generation produces other contaminants as well. For instance, power generation alone contributes to approximately 70% of SO₂, 20% of NO_x, and 40% of mercury emissions². These emissions do not only cause health problems to humans but also to the environment. The pollutant residence time is a key factor that must be considered when assessing the damage to the environment. This time may vary from few days to several years. When pollutants eventually fall back to the ground they can return in various forms such as rain, snow, fog, gases or particles². More detailed effects can arise. For SO₂ and NO_x, these interact with the atmosphere to form acidic mixtures, small particles and ozone². Acidic rain lowers the pH of lakes and rivers adversely affecting the health of the living organisms that depend on them. The small particles formed by SO₂ and NO_x decrease visibility and may cause severe respiratory problems in humans. Furthermore, NO_x emissions react in the presence of sunlight to form ozone which is a major component of smog². Finally, mercury may be deposited in water bodies and consumed by fish, fish-eating birds and mammals². Humans can then accidentally eat these contaminated animals and after a prolonged exposure suffer neurological damage.

One of the dominant types of power generation systems used today are gas turbines. Over the years, gas turbines have been an incredible source of reliability, efficiency, and have evolved to operate at temperatures as high as 2000K³. To counteract the high levels of toxic emissions in the earth's atmosphere carbon capture techniques have been considered. Oxy-combustion is a

carbon capture technique that uses oxygen instead of air when burning a hydrocarbon fuel. The advantage of an oxy-combustion system is that the products are carbon dioxide and steam, from which the steam can be condensed and the carbon dioxide sequestered meaning little to no emissions. However, flame temperature for an oxy-combustion system can exceed 3000K, which is well above current material operability limits of the combustor and gas turbine systems in use. To reduce flame temperature, fuel inlets are typically mixed with recycled carbon dioxide or other diluents, which results in overall lower temperature and system efficiency. In order to efficiently use oxy-combustion systems it is desired to operate at these high temperatures.

1.2 MAGNETOHYDRODYNAMIC POWER GENERATORS

A system capable of efficiently utilizing this energy with carbon capture are magnetohydrodynamic (MHD) generators, which are a type of direct power extraction. Most power generators used today involve a conversion to mechanical energy first, while MHD systems convert thermal energy directly to electrical power. These systems work similarly to mechanical generators where the motion of a metal conductor inside a magnetic field produces a current. However, in MHD generators the metal conductor is substituted by a hot, fast, conductive-gas⁴. Figure 1⁵ displays this main difference.

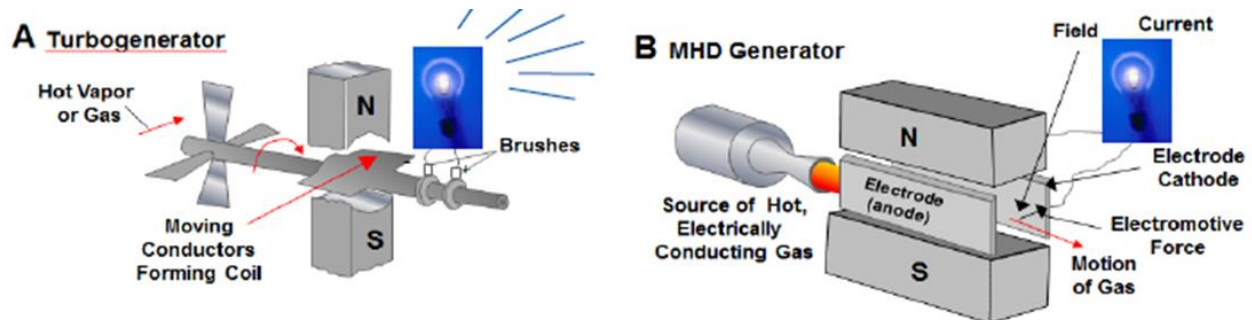


Figure 1: Turbogenerator vs. MHD generator

There are two types of MHD generators, closed cycle and open cycle. Closed cycle generators utilize heated, weakly-ionized, inert gases and are fairly documented in literature. On the other hand, open cycle generators are powered by fossil-fuel, ionized gases and have not been studied in depth. Ionization refers to stripping the molecules from their electrons leaving positively charged ions⁴. In order to increase the conductivity of the gases, scientist implement a technique known as seeding which consists of introducing particles of alkali-metals such as Cesium or Potassium in the flow. Other methods include heating or exposing the gases to X-rays or Gamma-rays⁴. As shown in Fig. 2⁴, conductivity does not increase linearly. About 90% of the conductivity can be achieved with 1% ionization in open cycle generators, and 0.1% in closed cycle generators⁶.

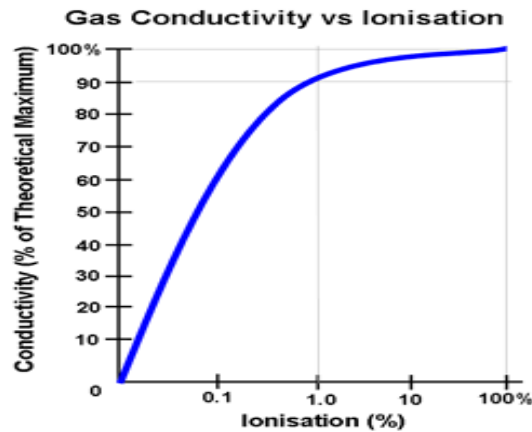


Figure 2: Gas conductivity vs. Ionization for open cycle MHD generators

1.3 FARADAY'S PRINCIPLE

Faraday first proposed the fundamental concept behind the MHD system in the early 1830's⁷. During his first studies he discovered that when a conductor passes through a magnetic field, it produces a current⁷. Using this concept, the first patented MHD system was created by Karlovitz and Halasz in the 1940's⁷. In general, MHD generators are an intricate system composed of three distinct parts. The first part of the system is the combustion chamber, which includes the fuel injector and igniter. As the gases fully combust, the products travel through a converging-

diverging nozzle that allows the gases to ionize and accelerate to supersonic velocities. After the nozzle, the gases are directed through an electromagnetic field, it is in this section that power is produced⁷. Following Fleming's Right Hand Rule, as the gaseous conductor moves through the magnetic field it generates an electrical current perpendicular to the magnetic field and the conductor's direction of flow, such phenomenon is illustrated in in Fig. 3⁴.

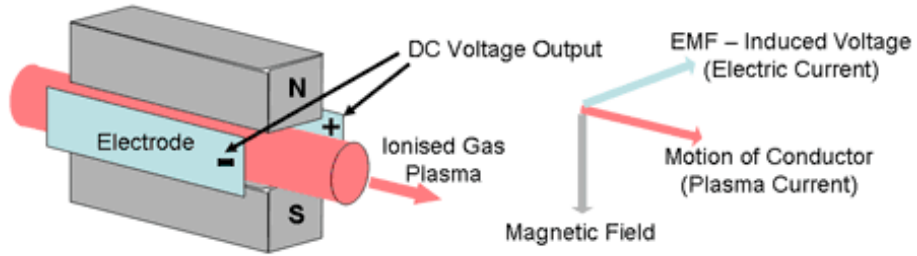


Figure 3: Fleming's Right Hand Rule

The Lorentz Force Law describes the effects of a charged particle traveling through a magnetic field. Where F stands for force acting on the particle, Q for the charge of the particle, v for velocity of the particle, and B for the magnetic field⁴.

$$F = Q \cdot (\vec{v} \times \vec{B}) \quad (1)$$

1.4 PREVIOUS WORK

MHD systems gained notoriety in the 19th century due to the potential of high efficiencies, mainly due to the high achievable temperatures above 3000K and absence of mechanical components⁸. These efficiencies typically vary between 10-20% due to thermal losses in the exhaust. Consequently, MHD systems are not practicable on their own, but when teamed with turbogenerators the combustion products can be used as the energy source to produce steam. Such hybrid configurations can reach efficiencies as high as 60%⁹. Way and Hundstad developed a design for a potassium seeded direct power extraction system, which produced a maximum of 10kW of energy when run for an interval of 3 seconds¹⁰. During this same time MHD power plants

began to emerge all over the world. The most well-known MHD power plant was constructed in the Soviet Union and was recorded to produce about 50 MW of power¹⁰. MHD power generation systems' efficiency is typically quantified in terms of enthalpy extraction ratio. Table 1 summarizes enthalpy extraction ratios found in some other studies^{11,12,13}.

Table 1: Enthalpy Extraction Percentages

| Source | Enthalpy Extraction (%) | Date Published |
|----------------------------|-------------------------|----------------|
| Sakhalin ¹¹ | 12 | 1999 |
| Avco-Everett ¹² | 16.6 | 1975 |
| AEDC ¹³ | 11 | 1982 |

$$\text{Enthalpy Extraction Ratio} = \frac{\text{Power Output}}{\text{Thermal Input}} \quad (2)$$

A sharp decrease in research of MHD systems was observed during the 20th century due to the increasing popularity of gas turbines and technical challenges for that period of time⁷. Technological advances in materials technology, as well as the high demand for alternative energy sources, have renewed the interest in MHD generators. Today, many studies focus on the use of computational models to predict the ability for gases exiting MHD combustors to conduct and produce electricity. Theoretical equations derived from these studies often contain assumptions that simplify the overall analysis and design of the system. Aithal and Ishikawa have presented computational models that are capable of predicting the optimum power extraction of the MHD generator using a code they developed^{14,15}. In the author's models, they were able to simulate the flow of the gases in the plasma state as they go through the magnetic field by implementing the Navier-Stokes equations^{14,15}. Bhadoria also showed, using a computational analysis, that oblique shocks form inside the MHD channel as the plasma passes through the magnetic field¹⁶. In this study, the oblique shocks were shown to aid in power generation.

Computational models for the cooling system of MHD generators have also been researched. A one dimensional heat transfer study was conducted by Wolfendale, utilizing

OpenFoam to model the fusion blanket in an MHD generator¹⁷. With this code the authors were able to predict the pressure loss and temperature profiles along the combustor walls. Combustion processes have also been simulated using the commercial software ANSYS-CFX to aid in the design of a rocket engine¹⁸. The combustion model proposed incorporates the Eddy-Dissipation models for oxygen-hydrogen combustion¹⁸. Utilizing this tool, the authors showed how the initial design was modified so that an adequate temperature profile could be obtained in the engine¹⁷.

Although some studies are available on the topic, overall there is a lack of research of computational models for the design of the combustion chamber, cooling unit, and nozzle section of open cycle MHD systems. Motivated by this, this paper aims to contribute to the current body of knowledge by presenting the computational models used in the design of an MHD combustor, conical converging diverging nozzle, and cooling system for a small-scale open-cycle MHD generator that operates using gaseous methane and oxygen.

Chapter 2: Theory

2.1 FUNDAMENTAL EQUATIONS

As Hernandez et. al. explains, the design process for the DPE combustor was the same of a typical rocket engine¹⁹. Its main components are a converging-diverging nozzle, a fuel manifold, and cooling channels. Figure 4 shows the test article's CAD drawing. The entire body of the combustor is made of a nickel-based super alloy; Inconel 718, due to its high yield strength at elevated temperatures. Manufacturing constraints dictated a 2° divergence angle. Following the nozzle there's a barrel section that should allow the addition of a seeding port in the future, if needed. Methane is injected into the fuel manifold and then distributed into 4 tangential ports. Oxygen is introduced through a coaxial port, transversal to the fuel orifices. The channel's hydraulic diameter was set to 2 mm in order to minimize pressure drop and reduce the required flow rate. It was possible to place a total of 6 channels around the combustor's geometry, thus enhancing the overall heat transfer capabilities. Detailed CADs with dimensions are found in Appendix B.

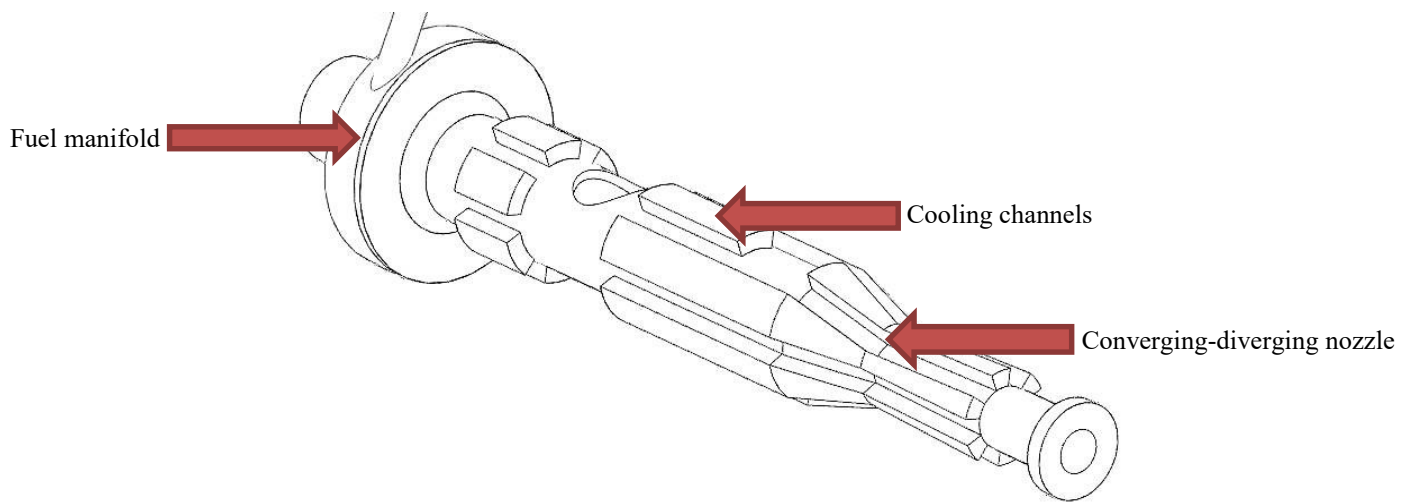


Figure 4: DPE combustor drawing

The governing mass and momentum equations, Eqs. (3-7)²⁰, were solved using software package ANSYS Fluent. All components utilized the mass and momentum equations hence they are presented first. Boundary conditions and details of the solving procedure for each component shown in Fig. 4 is presented in the following sections. Governing equations pertinent to each component are also presented in the following sections.

$$\frac{\partial \rho}{\partial t} + \nabla \cdot (\rho \vec{v}) = 0 \quad (3)$$

$$\frac{\partial}{\partial t}(\rho v) + \nabla \cdot (\rho \vec{v} \vec{v}) = -\nabla p + \nabla \cdot (\vec{\tau}) + \rho \vec{g} + \vec{F} \quad (4)$$

Where $\vec{\tau}$ is the stress tensor given by Eq. (5)²⁰.

$$\vec{\tau} = \mu \left[(\nabla \vec{v} + \nabla \vec{v}^T - \frac{2}{3} \nabla \cdot \vec{v} I) \right] \quad (5)$$

The mixing and shearing flow experienced in the injector along with high expected Reynolds numbers led to the assumption of turbulent flow. To model the turbulence, the standard k- ϵ model was implemented in the solver. The k- ϵ model introduces two extra transport equations for kinetic energy (k) and dissipation(ϵ), Eqs. (6,7)²⁰.

$$\frac{\partial}{\partial t}(\rho k) + \frac{\partial}{\partial x_i}(\rho k u_i) = \frac{\partial}{\partial x_j} \left[\left(\mu + \frac{\mu_t}{\sigma_k} \right) \frac{\partial k}{\partial x_j} \right] + G_k + G_b - \rho \epsilon - Y_M + S_k \quad (6)$$

$$\frac{\partial}{\partial t}(\rho \epsilon) + \frac{\partial}{\partial x_i}(\rho \epsilon u_i) = \frac{\partial}{\partial x_j} \left[\left(\mu + \frac{\mu_t}{\sigma_\epsilon} \right) \frac{\partial \epsilon}{\partial x_j} \right] + C_{1\epsilon} \frac{\epsilon}{k} (G_k + C_{3\epsilon} G_b) - C_{2\epsilon} \rho \frac{\epsilon^2}{k} - S_\epsilon \quad (7)$$

Table 2: Governing equations variables

| Symbol | Name |
|--------------|---|
| ρ | Density |
| ϵ | Dissipation rate |
| μ | Dynamic viscosity |
| g | Gravity |
| G_b | Kinetic energy generation due to buoyancy |
| G_k | Kinetic energy generation due to velocity |
| μ_t | Laminar viscosity |
| Y_M | Overall dissipation rate |
| P | Pressure |
| $\vec{\tau}$ | Stress tensor |
| k | Turbulent kinetic energy |
| v | Velocity |

2.1.1 Swirl Coaxial Injector

Methane is introduced to the combustion chamber through the fuel manifold shown in Fig. 5. The injection system uses a previously tested swirl injector which is responsible for creating a momentum vector that travels in a centripetal direction. This momentum vector is created due to the offset implemented in each injection point. The four tangential ports shown in Fig. 5 represent the fuel (methane) injectors. The oxidizer is introduced through the center port and shears the tangentially flowing fuel to create enhanced turbulence mixing behaviors before combustion.

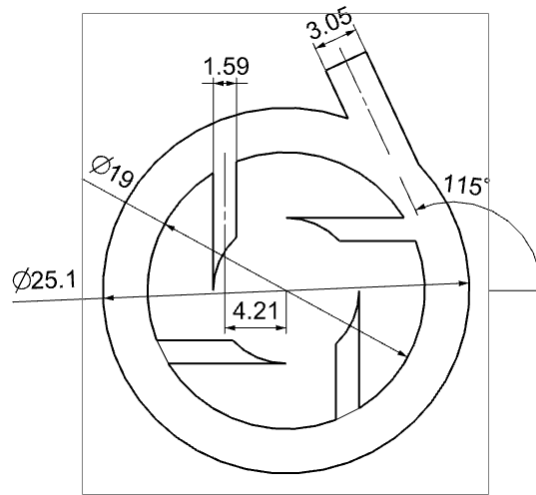


Figure 5: Swirl coaxial injector

While optimizing the injection system, many variables in the manifold geometry were manipulated using ANSYS Fluent. The results from the varied parameters improved flow in the injector. This included determination of equal velocity distribution along all four tangential inlets, uniform swirl velocities, and reduction of any low pressure regions (represented as voids) in the combustor. While modeling the injector it was observed that increasing the length to diameter ratio (L/D) proved beneficial to the flow characteristics previously mentioned. It was determined that an L/D of 4 would be sufficient to perform adequately. Originally the L/D was set to 0.75 and was steadily increased by set increments starting from 1 until the desired performance was achieved.

The length of the ports was constrained by manufacturing techniques that would be used to construct this same injector. Another variable that was analyzed was the path of injection (clockwise or counterclockwise). It was determined that clockwise was the most efficient configuration. Based on these observations, the final design was chosen and is shown in Fig. 5.

The manifold dimensions were initially in imperial units. Therefore, translation to the metric system is displayed with two significant figures for better accuracy. The width of the manifold ring is 6.1 mm; the inner diameter is 19 mm while the outer diameter is 25.1 mm. Every orifice is 1.59 mm in diameter with an offset distance of 4.21 mm from the center. The inlet pipe is 3.05 mm in diameter and is introduced at 115° in respect to the x-axis. Furthermore, the injector's 310 kPa pressure drop was quantified using Eq. (8)²¹.

$$q = YCA \sqrt{\frac{2g(144)\Delta P}{\rho}} \quad (8)$$

Table 3: Injector pressure drop variables

| Symbol | Name |
|------------|---------------------|
| A | Area |
| ρ | Density |
| Y | Expansion factor |
| C | Flow coefficient |
| g | Gravity |
| ΔP | Pressure difference |

Early models angled the inlet plane 45° in respect to the x-axis (Fig. 6). This configuration proved to have poor distribution capabilities as it produced large voids. The issue was attributed to the collision methane suffered as it entered the manifold. The abrupt shock disturbed the fluid's momentum and consequently slowed it down considerably. Later versions repositioned the inlet plane tangential to the ring manifold, and eventually to 115° in respect to the x-axis.

2.1.1.1 Early Swirl Coaxial Injector with Ring Manifold

Figure 9 displays the first injector design which incorporated a ring manifold. As previously discussed, this configuration proved to be inefficient at evenly distributing the fuel to

all four tangential ports. The geometry was optimized for a combustor with much thicker walls. Consequently, it was able to afford a longer L/D ratio. Once it was determined that the DPE combustor would employ a 1 mm wall thickness the L/D was adapted accordingly. Other dimensions that evolved included the ring manifold width and the inlet plane angle. A feature that proved to be ineffective and eventually removed was a small indentation 3.24 millimeters in diameter intended to redirect the flow of the fuel to the orifices. It was determined that the crucial dimensions that could not be modified were the orifice diameter for the four tangential ports, and their respective offset.

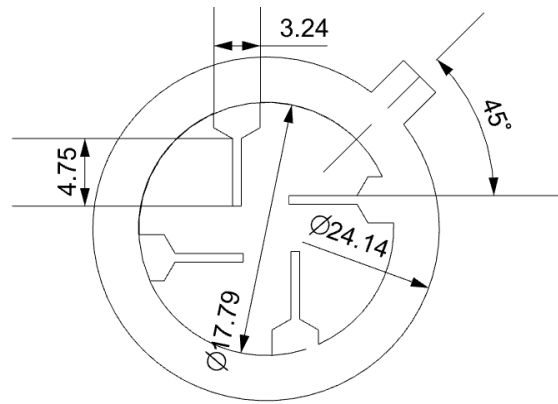


Figure 6: Early swirl coaxial injector with ring manifold

2.1.2 Converging-Diverging Nozzle

The combustion product's properties are highly affected by the nozzle's geometry. The combustion chamber, throat, and exit diameters are 10, 3.68, and 5 mm, respectively. The converging section has a half angle of 15° and a length of 11.9 mm. The diverging section has a half angle of 2° and a length of 20 mm. Early designs of the combustor incorporated a divergence angle of 15° , as it is the standard configuration for rockets. However, due to the size of this specific combustor, such angle had to be modified in order to increase the overall nozzle length. Otherwise, many manufacturing challenges would arise, such as machinability and/or cost. The barrel section intended for seeding is 10.7 mm in length. As previously explained, the function of seeding is to

activate the conductivity of the weakly ionized combustion products. Figure 7 shows a cross-sectional view of the test article.

Such dimensions, in conjunction with the DPE combustor's operating conditions (discussed later in this chapter) yielded an under-expanded nozzle. Thus sacrificing velocity in order to preserve an elevated exit temperature. A conventional DPE system requires flame temperatures between 2800–3000K to improve electrical conductivity. Furthermore, velocities of 1800 – 2000 m/s are required to increase the energy extraction potential. If the combustion products do not meet both requirements energy extraction is not possible.

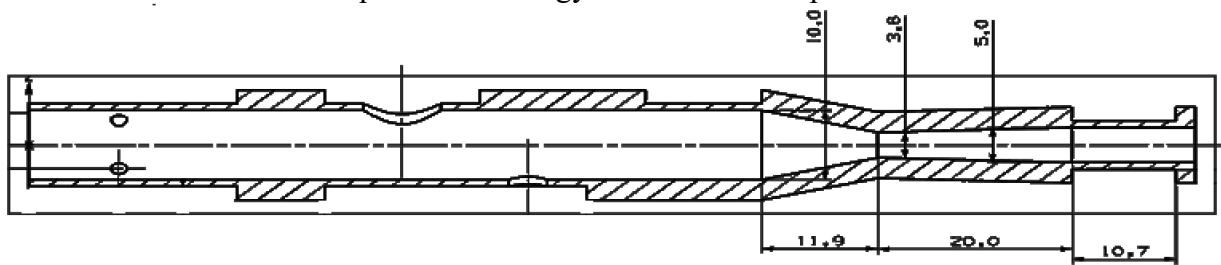


Figure 7: DPE combustor and converging-diverging nozzle

For simplicity, initial assumptions included constant chamber pressure and isentropic conditions. In order to obtain the exit temperature and velocity from the nozzle, NASA chemical equilibrium with applications (CEA) software was utilized. CEA was developed by the Lewis Research Center and is widely used for aerodynamic and thermodynamic applications. The program obtains its information from independent databases, from which it computes chemical reactions for any specified mixture and defines its thermodynamic and transport properties²². The one dimensional code assisted in the determination of a baseline of expected temperatures, products, and pressures in the system. The CEA code was run assuming an equivalence ratio of 1.14, chamber pressure of 758.42 kPa, and an exit to throat area ratio of 1.85. Combustion products were run using the assumption of frozen equilibrium. When implementing these conditions, an exit temperature of 2874 K and velocity of 2119 m/s were calculated. Full results can be found in Appendix A.

A Fluent non-premixed combustion model was used and results compared with CEA. This model attempts to simplify the thermochemistry to the mixture fraction. The mixture fraction, represented by f , is the mass ratio of burnt and unburnt elements²³.

$$f = \frac{Z_i - Z_{i,ox}}{Z_{i,fuel} - Z_{i,ox}} \quad (9)$$

By using this model species were determined from predicted mixture fraction quantities. Moreover, the relationship between turbulence and chemistry is modeled using a Probability Density Function (PDF). The PDF is computed before the simulation starts using the elements' initial conditions, which for this study is one mole of methane and two moles of oxygen. By performing these operations, the overall computational time was reduced.

For this model the fluids were assumed to have equal diffusivities, thus the species equations were condensed to a single mixture fraction function. Due to the fact that elements are conserved in chemical reactions, it is possible to cancel the reaction terms in the species equations. This assumption is typically suitable for turbulent flow only, as the turbulent convection overcomes molecular diffusion²³. The Favre mean mixture fraction is denoted as:

$$\frac{\partial}{\partial t}(\rho \bar{f}') + \nabla(\rho \vec{v} \bar{f}) = \nabla \left(\frac{\mu_l + \mu_t}{\sigma_t} \nabla \bar{f} \right) + S_m + S_{user} \quad (10)$$

Fluent solves for the conservation equation for the mixture fraction variance, which is obtained by expanding Eq. (10)²³ to:

$$\frac{\partial}{\partial t}(\rho \overline{f'^2}) + \nabla(\rho \vec{v} \overline{f'^2}) = \nabla \left(\frac{\mu_l + \mu_t}{\sigma_t} \nabla \overline{f'^2} \right) + C_g \mu_t (\nabla \bar{f})^2 - C_{d\rho} \frac{\varepsilon}{k} \overline{f'^2} + S_{user} \quad (11)$$

Table 4: Non-premixed model variables

| Symbol | Value |
|---------------|----------------------------|
| ρ | Density |
| ε | Dissipation rate |
| μ_l | Laminar viscosity |
| Z_i | Mass fraction of element i |
| Z_{fuel} | Mass fraction of fuel |
| Z_{ox} | Mass fraction of oxygen |
| f | Mixture fraction |
| k | Turbulent kinetic energy |
| μ_t | Turbulent viscosity |
| v | Velocity |

2.1.2.1 Simplified Combustor Model

The model displayed in Fig. 8 is a simplified version of the DPE combustor and was used as a starting point for the converging-diverging nozzle simulation. The design neglected the characteristic offset associated with the swirl-coaxial injector and employed a simple cross injector instead. Additionally, the span of the combustion chamber was considerably longer as early simulations exhibited issues achieving complete combustion. The nozzle had a converging half angle of 20° and a diverging half angle of 7° , making the overall length 5 mm. Once satisfactory results were achieved a more elaborate model was developed.

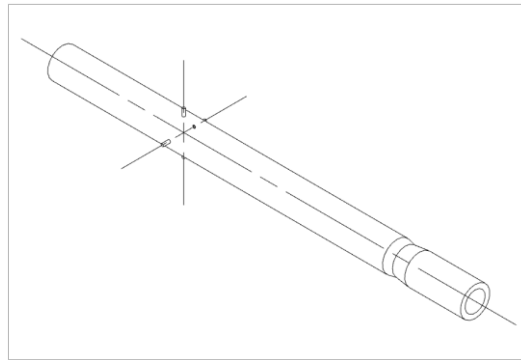


Figure 8: : Simplified DPE combustor

2.1.2.2 DPE Combustor Concept

The DPE combustor was based off of a previously existing design. Such system was only required to operate for short periods of time in the magnitude of seconds. For that reason, the walls were much thicker as heat dissipation was not an issue of concern. The design employed a fuel manifold which distributed the flow into 4 external tubes, while the oxidizer was introduced through the lateral. Figure 9 shows one of the many early concepts of the DPE combustor. The fuel distribution system was a hybrid configuration between the ring manifold and the original external tubes manifold. The oxygen port was modified to be introduced coaxially. Initially, the cooling system only incorporated one inlet and one outlet, later designs added another pair for distribution purposes.

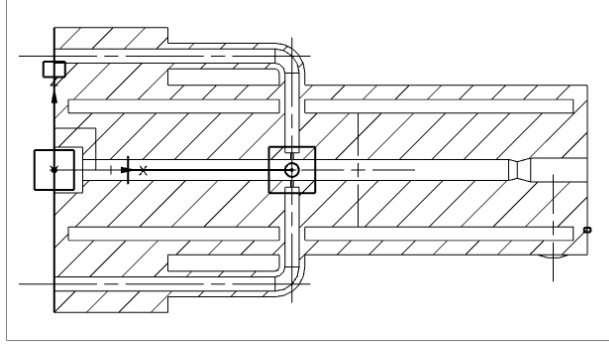


Figure 9: DPE combustor concept

2.1.3 Cooling System

The yield strength of Inconel 718 begins to decline after it exceeds 540 °C. Since the DPE combustor is intended to operate for an indefinite amount of time, the cooling system is required to maintain the wall temperature between 500–540 °C at all times. Expecting temperatures close to 3000K inside the combustion chamber, a geometry that balanced both thermal conductivity and structural strength was needed. It was found that extending the wall thickness reduced static stress but in consequence increased thermal stress. In order to find the optimal thickness for the combustor, a simplified version of the Bartz correlation and the Colburn equation were used²⁴. The Bartz correlation predicts the heat transfer coefficient at different points of the nozzle, while the Colburn equation makes an analogy between heat, momentum and mass transfer. However, it has been argued that the Bartz correlation tends to overestimate the convective heat transfer coefficient between 20-40% as a result of flow instabilities, combustion efficiency variations, and impurities deposits that act as insulators^{24,25}. To correct the over-prediction, the initial heat transfer coefficient value of 4544 W/m²-K was reduced to 2726, yielding a heat flux of 6.86 MW/m² at the throat. Theory states that this is the highest heat flux location due to its small surface area. Assuming a wall temperature of 525 °C and a wall thickness of 1 mm, resulted in a mechanical and thermal combined stress of ~610 MPa. At such temperature Inconel has a yield strength of 995 MPa. Equation (11)²⁴ makes a relationship between mechanical stress and thermal stress to the wall

thickness, heat flux, and material properties. Appendix A goes more into detail regarding how this formula was employed.

$$S_c = \frac{(p_{co}-p_g)R}{t} + \frac{Eaqt}{2(1-\nu)k} \quad (12)$$

The Sieder-Tate equation (Eq. 13)²⁴ was used to better understand the relationship between required coolant velocity and hydraulic diameter. Calculations revealed that a larger hydraulic diameter required higher coolant velocities.

$$Nu = 0.027Re^{.8}Pr^{.33} \left(\frac{\mu}{\mu_w} \right)^{.14} \quad (13)$$

Table 5: Combined stress & Sieder-Tate equation variables

| Symbol | Name |
|----------|--|
| a | Coefficient of thermal expansion |
| p_g | Combustion-gas pressure |
| p_{co} | Coolant pressure |
| μ | Coolant viscosity at bulk temp |
| μ_w | Coolant viscosity at coolant sidewall temp |
| E | Modulus of elasticity |
| Nu | Nusselt number |
| ν | Poisson's ratio |
| Pr | Prandtl number |
| R | Radius of inner shell |
| Re | Reynolds number |
| k | Thermal conductivity |
| t | Wall thickness |

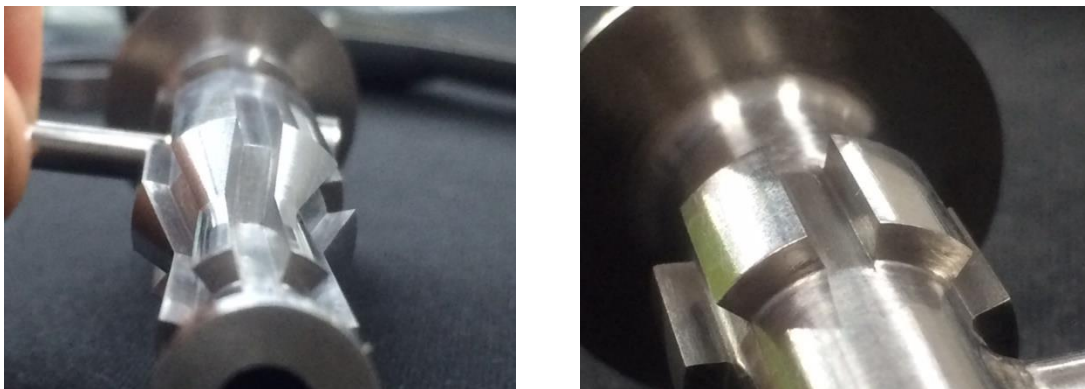


Figure 10: Cooling channels

In order to enhance the cooling capabilities, the DPE combustor contains six channels (Shown in Fig. 10) two millimeters in height and width. Such dimensions minimize the pressure drop and reduce the required flow rate. The complex geometry of the channels was added to the combustor using a manufacturing technique known as Electrical Discharge Machining (EDM). The process consists of removing material from the work-piece using electrical discharges.

Water was selected as the coolant due to its low viscosity, heat capacity, and abundance. Nevertheless, due to its relatively low boiling temperature, the water must be introduced pressurized to increase its saturation temperature. It was found that the required flow rate to effectively cool down the walls of the oxy-fuel combustor was approximately 16 LPM, for which a high-head, low-flow pump was selected. Appendix A shows how these results were manually validated. The water flows in a counter flow configuration entering near the exit of the nozzle and exits near the injector. Figure 11 shows the water inlet and exit ports. The chamber has various obstructions to allow temperature sensors, pressure instrumentation, and ignition ports to pass through. The elaborate geometry of the test article required an ANSYS Fluent model to better understand the maximum pressure and velocity the coolant could experience before cavitation occurred.

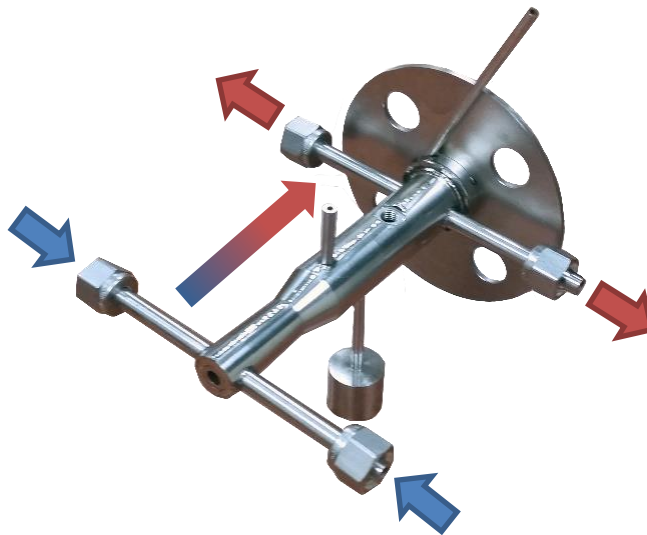


Figure 11: Cooling Jacket

In order to simulate the heat transfer occurring in the system, the energy equation is utilized, Eq. (14)²⁶.

$$\frac{\partial(\rho E)}{\partial t} + \nabla \cdot [\vec{V}(\rho E + p)] = \nabla \cdot [k_{eff} \nabla T - \sum_j h_j J_j + (\vec{\tau}_{eff} \cdot \vec{V})] + S_h \quad (14)$$

Heat transfer due to conduction, species transport, and viscous dissipation were all considered for the current project²⁶. The heat conduction through the walls and the heat transfer to the water is also modeled. Heat convection occurring between the fluid and walls assumed the cooling fluid (water) was incompressible and neglected kinetic energy and viscous dissipation²⁶. These assumptions further simplified the energy equation and yielded Eq. (15)²⁶.

$$\frac{\partial T}{\partial t} + u \frac{\partial T}{\partial x} + v \frac{\partial T}{\partial y} = \frac{\lambda}{\rho c_p} \frac{\partial^2 T}{\partial x^2} + \frac{\lambda}{\rho c_p} \frac{\partial^2 T}{\partial y^2} \quad (15)$$

Table 6: Cooling system model variables

| Symbol | Name |
|-----------|-----------------------------|
| ρ | Density |
| J_j | Diffusion flux of species j |
| k_{eff} | Effective conductivity |
| h_j | Enthalpy for species j |
| P | Pressure |
| C_p | Specific heat |
| T | Temperature |
| λ | Thermal conductivity |
| t | Thickness |
| V | Velocity |
| S_h | Volumetric heat source |

2.1.3.1 Simplified Cooling System Model

Developing the simulation for the cooling system proved to be a hard and challenging task. Therefore, a simplified geometry which mimicked coolant flow through 2 mm by 2mm channels was designed to aid as a stepping stone towards a more accurate model. Such model neglected the two 4 mm obstructions for the static pressure and temperature measurement devices, as well as the

8 mm obstruction designated for the spark-igniter port. The geometry also lacked the internal manifold where the water distributes.

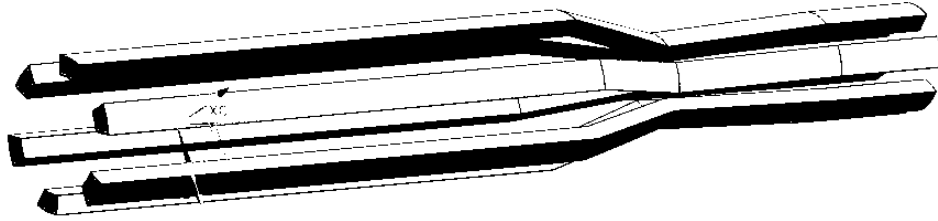


Figure 12: Simplified cooling system model

2.2 MESH

The following section describes the mesh properties for the final models only.

2.2.1 Swirl Coaxial Injector

The fuel injector system mesh was created using the ANSYS Workbench meshing tool and modified by the ANSYS Fluent adapt region function. The mesh contained a combination of triangular and quadrilateral elements with inflation layers added on the injector walls as shown in Fig. 13. The mesh originally contained 909 nodes with 788 elements and after the adaption the number increased to 12,470 nodes with 25,255 elements. The mesh has a minimum orthogonal quality of 0.111, maximum orthogonal quality of 0.999, minimum aspect ratio of 1.0035, and maximum aspect ratio of 23.4.

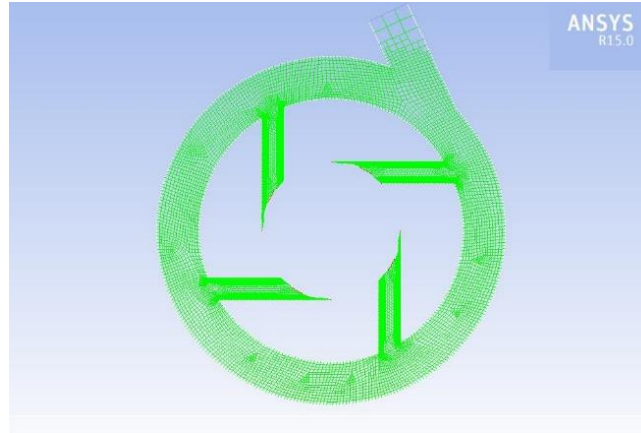


Figure 13: Swirl coaxial injector mesh

2.2.2 Converging-Diverging Nozzle

The mesh utilized for the combustion simulation was generated by the ANSYS meshing tool and was composed of 126,236 elements. In order to improve accuracy, while maintaining a relatively low number of elements to save computing time, the mesh was refined in strategic places. One of these areas was located at the four injection ports and its surrounding areas, where the methane is introduced into the system and mixes with the oxygen flowing coaxially. A second refined area included the throat, nozzle's diverging section, and barrel section in order to obtain accurate exit properties.

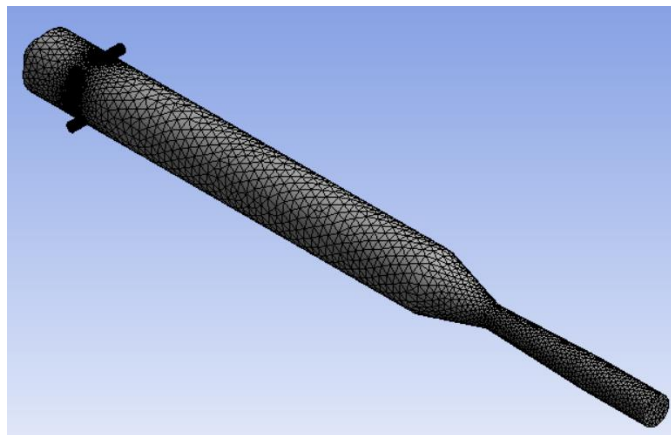


Figure 14: Combustor and converging-diverging nozzle mesh

2.2.3 Cooling System

The mesh that was implemented for the cooling system consisted of both quadrilateral and tetrahedral elements, for a total of 149,734 elements. After constructing the mesh, the geometry was split into three distinct walls. The first wall was located around the combustion chamber. The second and third walls were located around the nozzle and exit sections, respectively. The inlet of the water was located near the nozzle exit while the water outlet was near the fuel manifold. The geometry for the fluid domain of the water was developed utilizing the Siemens NX CAD software and is shown in Fig. 15.

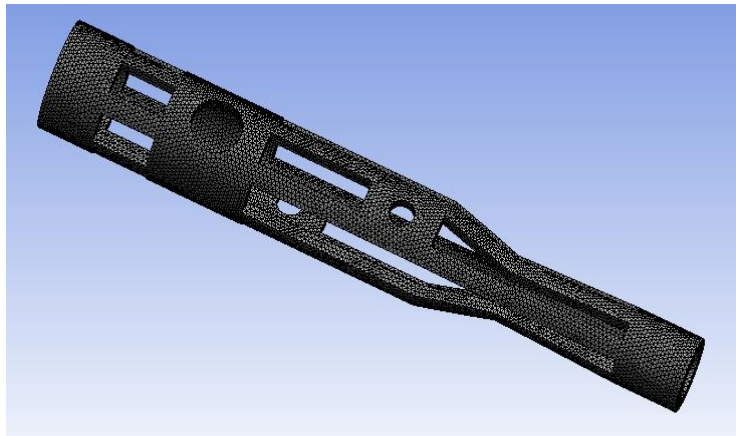


Figure 15: Cooling system mesh

2.3 BOUNDARY CONDITIONS

The boundary conditions for the final models can be seen in Tables 7-9. If not specified, values were left at their default setting.

2.3.1 Swirl Coaxial Injector

The fuel mass flow rate was translated into terms of velocity as the injector model refused to accept “mass flow” for the inlet condition. A factor that played a vital role in the success of this model was the inflation layers in the injection ports. Prior to implementing this feature, it was common for the simulation to diverge before it completed the specified number of iterations.

Table 7: Boundary conditions for the swirl coaxial injector

| Section | Input |
|-------------------------|--|
| General | Gravitational acceleration - 9.81 m/s ² |
| Models | Multiphase – Volume of fluid Viscous – Standard k-epsilon |
| Materials | Methane: <ul style="list-style-type: none"> • Density – 0.6654 kg/m³ • Cp – Piecewise-polynomial |
| Phases | Primary – Air Secondary – Methane |
| Boundary conditions | Mixture inlet: <ul style="list-style-type: none"> • Velocity - 200 m/s • Hydraulic diameter – 3.05 mm Methane inlet: <ul style="list-style-type: none"> • Volume fraction – 1 Mixture outlet: <ul style="list-style-type: none"> • Pressure - 657.14 kPa • Hydraulic diameter – 1.59 mm |
| Solution initialization | Standard – Inlet |

2.3.2 Converging-Diverging Nozzle

The converging-diverging nozzle model took a considerable amount of time to complete. Often times the simulation would diverge immediately. In other occasions it would complete a vast amount of iterations, but eventually diverge before reaching steady state. Modifying the “initial values” under solution initialization was found to solve the issue. The temperature and velocity were specified to an approximate middle point between the initial and (expected) final values. Additionally, some under-relaxation factors were applied per suggestion of the official ANSYS Fluent Tutorial Guide. Appendix A describes how the fuel and oxidizer mass flow rates were determined.

Table 8: Boundary conditions for the converging-diverging nozzle

| Section | Input |
|-------------------------|---|
| Models | Energy – On Viscous – Standard k-epsilon Radiation – P1 Species – Non-premixed combustion <ul style="list-style-type: none"> • Inlet diffusion – On • Compressibility effects – On • Fuel stream reach flammability limit - 0.23 • Mass fraction of CH₄ – 1 • Mass fraction of O₂ - 1 |
| Materials | PDF mixture <ul style="list-style-type: none"> • Absorption coefficient – wsggm-domain-based |
| Boundary conditions | Fuel inlet: <ul style="list-style-type: none"> • Mass flow rate - 0.25025 g/s per orifice • Initial gauge pressure – 657.14 kPa • Hydraulic diameter – 1.59 mm • Mean mixture fraction – 1 Oxidizer inlet: <ul style="list-style-type: none"> • Mass flow rate – 3.495 g/s • Initial gauge pressure - 657.14 kPa • Hydraulic diameter – 10 mm Outlet: <ul style="list-style-type: none"> • Hydraulic diameter – 5 mm • Backflow total temperature – 1500 K Wall: <ul style="list-style-type: none"> • Temperature - 525 K |
| Solution Controls | Pressure - 0.9 Body forces - 0.9 Momentum - 0.4 Turbulent kinetic energy - 0.7 P1: 0.5 |
| Solution initialization | Standard – Inlet Gauge pressure - 657.14 kPa X-velocity - 1000 m/s Temperature: 1650 K |

2.3.3 Cooling System

Obtaining negative pressure values was a reoccurring problem in the cooling system simulation. The issue was resolved by selecting a “target mass flow rate” condition for the outlet, instead of the conventional “outlet pressure”.

Table 9: Boundary conditions for the cooling system

| Section | Input |
|-------------------------|--|
| Models | Energy – On Viscous – Standard k-epsilon |
| Materials | Water |
| Boundary conditions | Inlet: <ul style="list-style-type: none">• Gauge total pressure - 862.09 kPa• Initial gauge pressure - 620.53 kPa• Hydraulic diameter - 2.58 mm Outlet: <ul style="list-style-type: none">• Gauge pressure - 101.3 kPa• Target mass flow rate - 283 g/s• Hydraulic diameter – 2.58 mm Wall: <ul style="list-style-type: none">• Combustion chamber: 0.8 MW/m²• Nozzle: 6.86 MW/m²• Barrel: 3.61 MW/m² |
| Solution initialization | Standard – Inlet |

Chapter 3: Results and Discussion

The results for the final models and a few concepts are discussed in this chapter in order to demonstrate how the design process evolved and evaluate improvements.

3.1 SWIRL COAXIAL INJECTOR

3.1.1 Velocity and Pressure

Figure 16 reveals a 48 kPa pressure drop inside the fuel manifold. The pressure shows to be evenly distributed among the four ports for this given 4 L/D ratio. Increasing the L/D ratio resulted in better flow distribution within the injectors both with respect to velocity and pressure. However, it also increased pressure drop and material cost. The L/D ratio was incrementally increased until results were satisfactory. Figure 17 presents the velocity contour, even though it might not appear equally distributed a surface integral analysis confirmed constant velocity of approximately 190 m/s at all ports. The main inlet was positioned between two injectors, being closer to one would vastly disrupt the distribution efficiency and exhibit bias results towards that particular orifice. Tangential inlets delivered the least amount of fuel to the closest injector whereas radial inlets delivered too much.

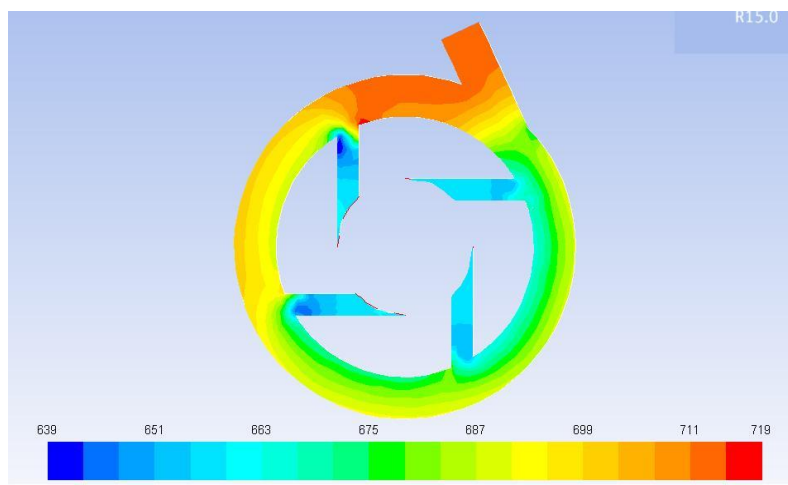


Figure 16: Fuel injector static pressure contour, units shown are in kPa

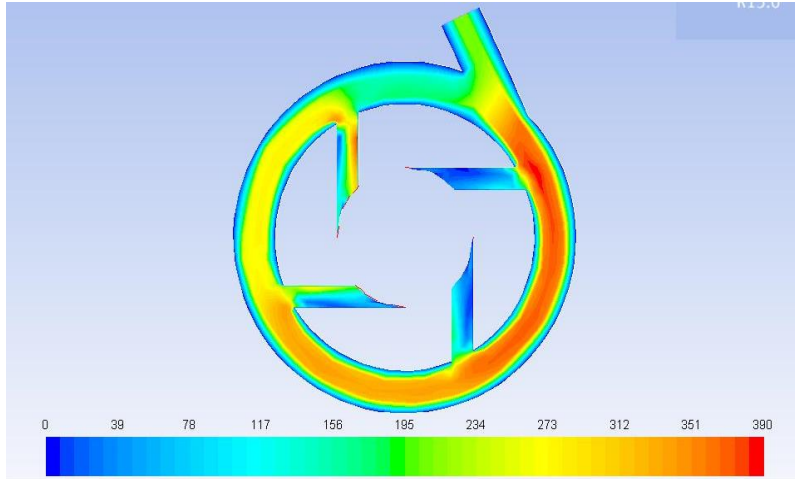


Figure 17: Fuel injector velocity contour, units shown in m/s

3.1.2 Volume Fraction

The volume fraction diagram was an important tool as it provided fluid flow insight at any given time. It was determined that the required time to fill the system was 4.45 ms. Figures 18 (a-e) show the methane flow at 0.1, 0.5, 1, 2 and 4.45 ms, respectively. The volume fraction diagrams illustrate how the flow propagates through the injector manifold filling each injector from the upper right and upper left to the bottom. The final remnants of air exit the fuel manifold at 4.5 ms.

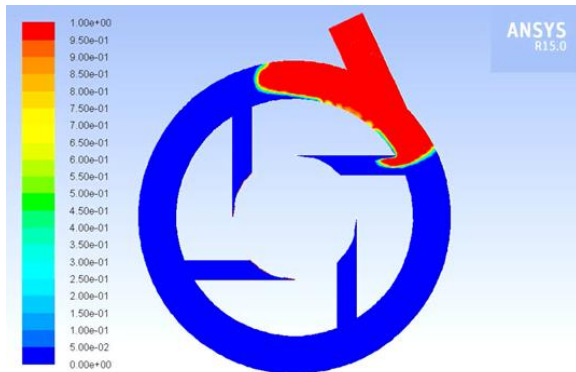


Figure 18(a): Injector volume fraction contour of methane at 0.1 ms

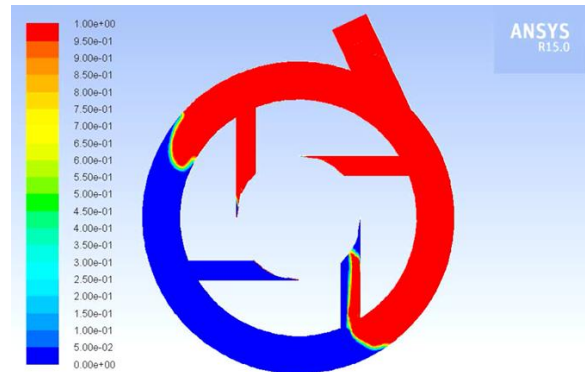


Figure 18(b): Injector volume fraction contour of methane at 0.5 ms

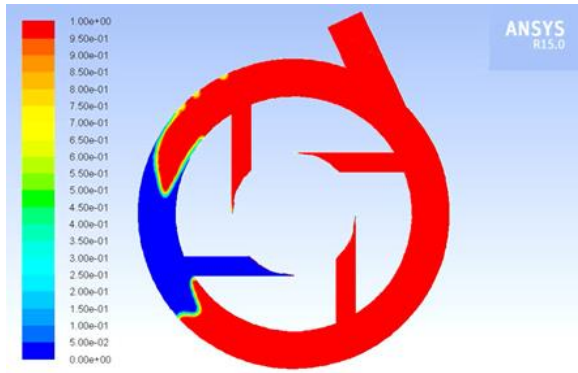


Figure 18(c): Injector volume fraction contour of methane at 1 ms

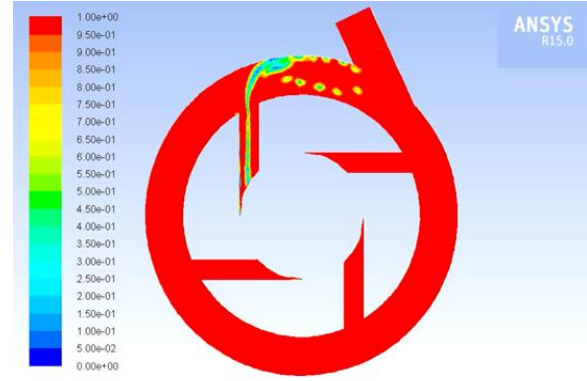


Figure 18(d): Injector volume fraction contour of methane at 2 ms

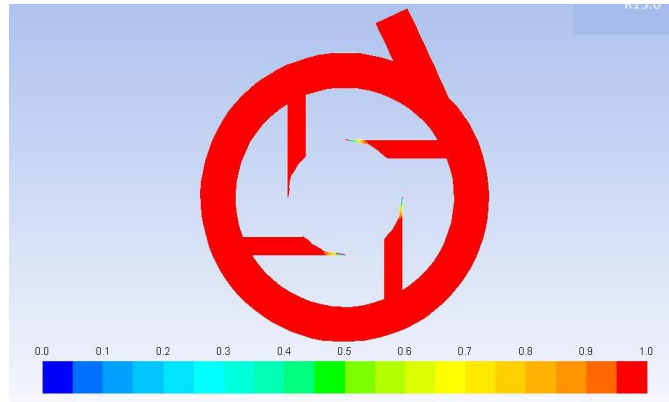


Figure 18(e): Injector volume fraction contour of methane at 4.45 ms

3.1.3 Swirl Coaxial Injector Early Design

The pressure contour exhibits a high pressure region in the orifice closest to the inlet port. The pressure in the three remaining orifices remained relatively similar. Even though the velocity might appear equal in all orifices, the fuel does not flow all the way around the manifold. The

velocity contour, shown in Fig. 19, reveals a large area in the opposite end of the inlet port with no velocity.

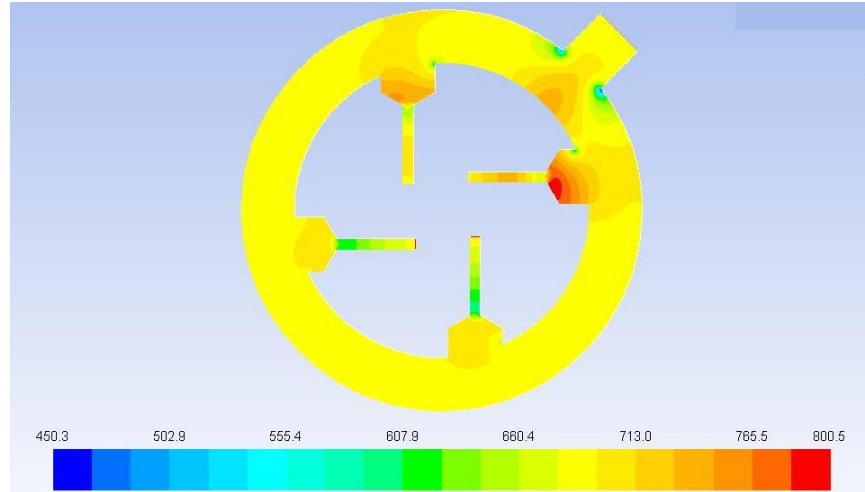


Figure 19: Early fuel injector static pressure controur, units shown are in kPa

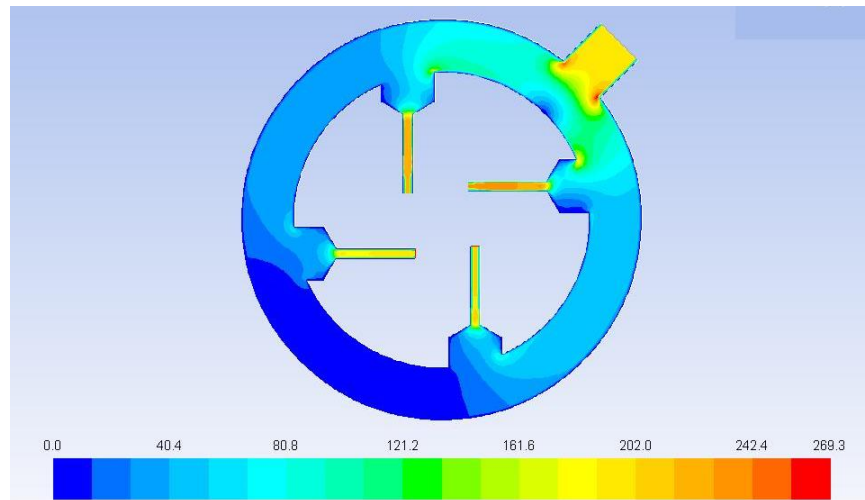


Figure 20: Early fuel injector velocity contour, units shown are in m/s

Figure 21 shows the methane volume fraction for the first swirl coaxial injector with a ring manifold. The image on the left was captured at 1 ms, while the image on the right at 3 ms. Little to no change was observed after 3 ms, which means the fuel distribution did not improve. Large amounts of voids can be observed in the contours. This configuration would have resulted in

combustion instabilities and/or ignition problems. As stated before, the poor distribution efficiency was attributed to the disturbance in the fluid's momentum when it enters the manifold and collides with the wall.

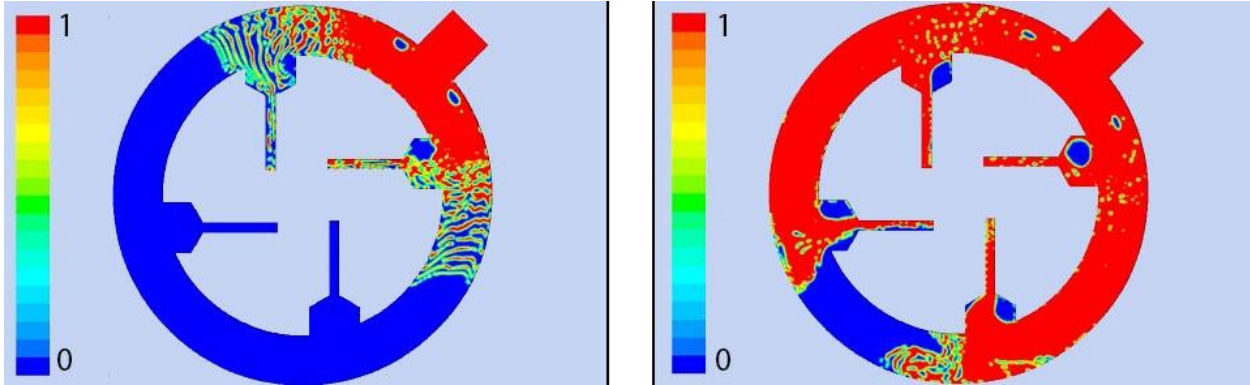


Figure 21: Early injector volume fraction contours of methane at 1 and 3 ms

3.2 CONVERGING-DIVERGING NOZZLE

3.2.1 Velocity and Temperature

Figures 22 and 23 show the velocity and temperature contours. The values were similar to those obtained from the NASA CEA code. An exit velocity of 1920 m/s and an exit temperature of 2725K was computed. Table 10 presents the comparison between the two sets of results.

Table 10: Results comparison between CEA and Fluent model

| | CEA Results | Fluent Results |
|-----------------|--------------------|-----------------------|
| Velocity (m/s) | 2119 | 1920 |
| Temperature (K) | 2874 | 2725 |

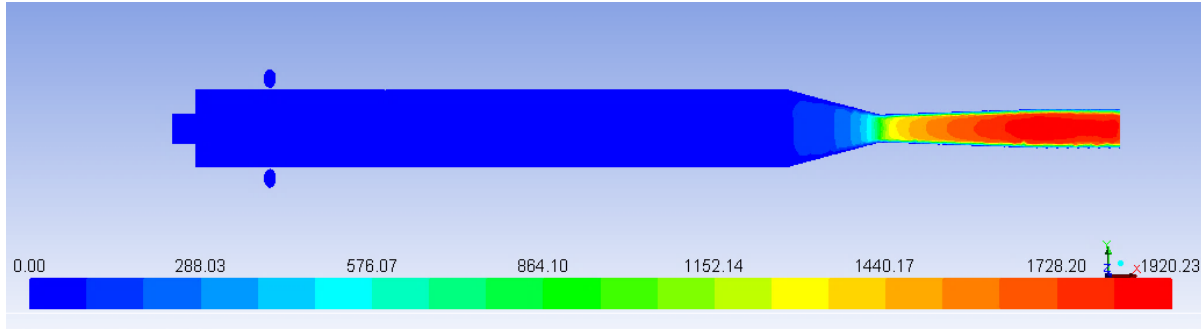


Figure 22: Velocity contour with combustion, units shown are in m/s

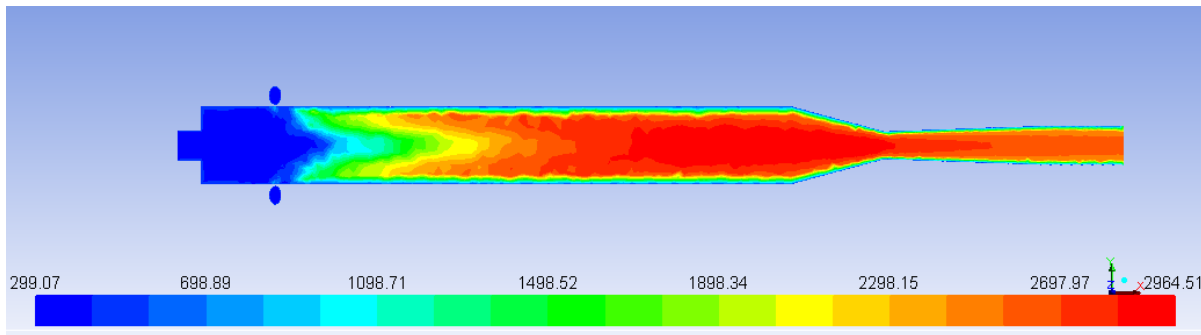


Figure 23: Temperature contour with combustion, units shown are in K

Even though the same boundary conditions were specified in both programs, it had been anticipated that Fluent's results would be more realistic and therefore lower. The basis for that prediction was that CEA is a one-dimensional isentropic case, contrary to Fluent which is a three-dimensional model that takes into account other factors such as thermal and friction losses.

As expected from theory, Fig. 22 displays subsonic flow at the converging section of the nozzle, sonic flow at the throat, and supersonic flow in the diverging section. The mixing region can easily be recognized in the temperature contour. Shortly after the methane injector ports temperature increases very rapidly, reaching up to 2965K at the combustion chamber. Temperature then decreases again in the diverging section of the nozzle. For this specific system, the idealistic exit properties for the gases were defined as 2000 m/s at 3000K, with a $\pm 10\%$ tolerance. The lowest velocity value from the two programs was within 4%, while the lowest temperature result was within 9%. Therefore, both requirements were successfully achieved.

3.2.2 Vectors

Fuel is introduced through the four orifices creating a centripetal effect in the counterclockwise direction. Figure 24 shows the methane velocity vectors as it enters the combustion chamber. The center region of the image appears to have little to no content of methane, result of the oxygen being injected coaxially. Furthermore, other elements are expected to be present in that area as it is the mixing point and where the combustion zone begins.

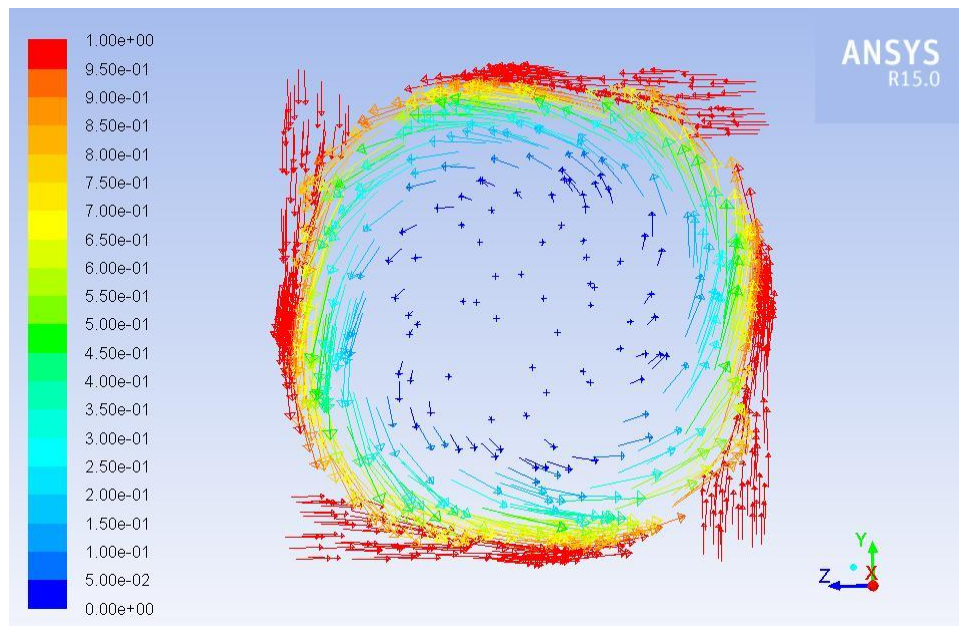


Figure 24: Methane velocity vectors

3.2.3 Methane and Oxygen Path-lines

The methane and oxygen path-lines can be observed in Figures 25 and 26, respectively. They serve as complementary images to Fig. 24 while analyzing the behavior of the fluids once they have been introduced into the combustion chamber. Methane continuously swirls following the contour of the wall. Oxygen enters straight from the inlet port located on the far left and collides with the methane swirl. The volume fraction of both the fuel and oxidizer gradually decrease after the mixing point due to the chemical reaction.

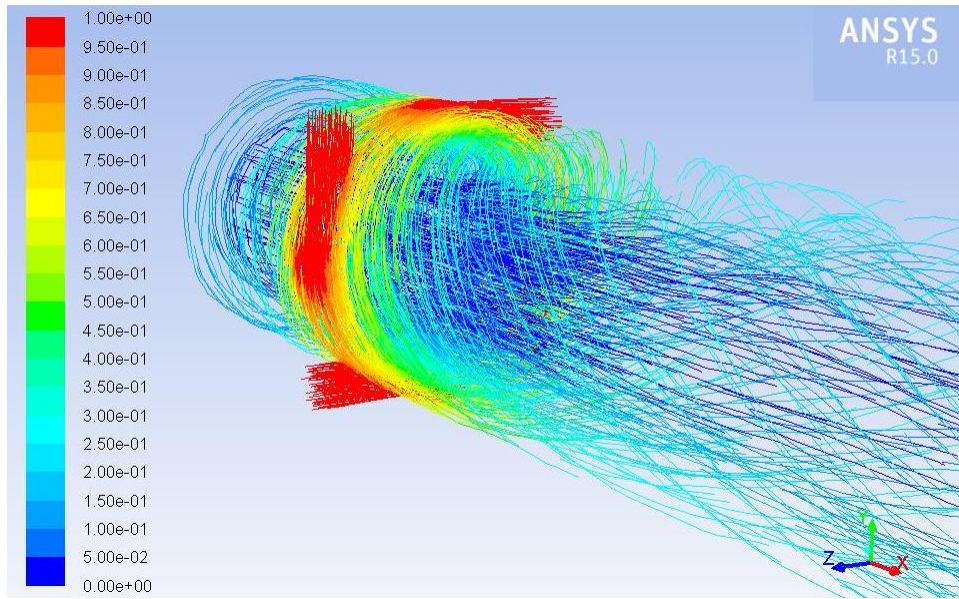


Figure 25: Methane pathlines

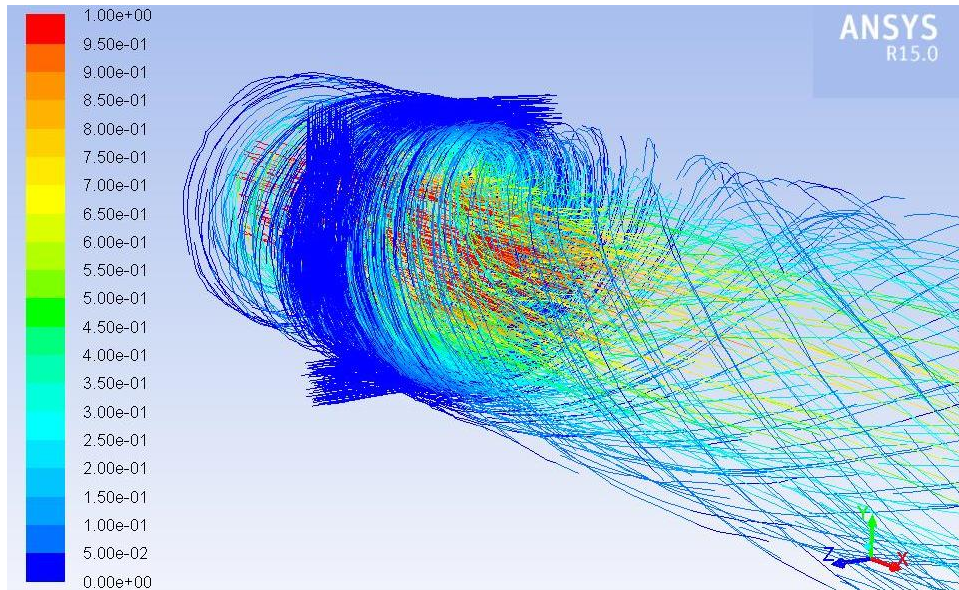


Figure 26: Oxygen pathlines

3.2.4 Boundary Layer

As a fluid flows over an object the particles adjacent to the surface stick to the surface. Consequently, the particles closest to the object get slowed down due to the collisions with the

stagnant particles²⁶. Such occurrence keeps decreasingly repeating to the neighboring molecules. In rockets this creates a film known as boundary layer, where the velocity varies from zero at the walls to the actual stream value at the center on the nozzle²⁷. The DPE combustor's boundary layer is shown in Fig. 27. The velocity fluctuates from zero at the surface to 1920 m/s at the center of the diverging section.

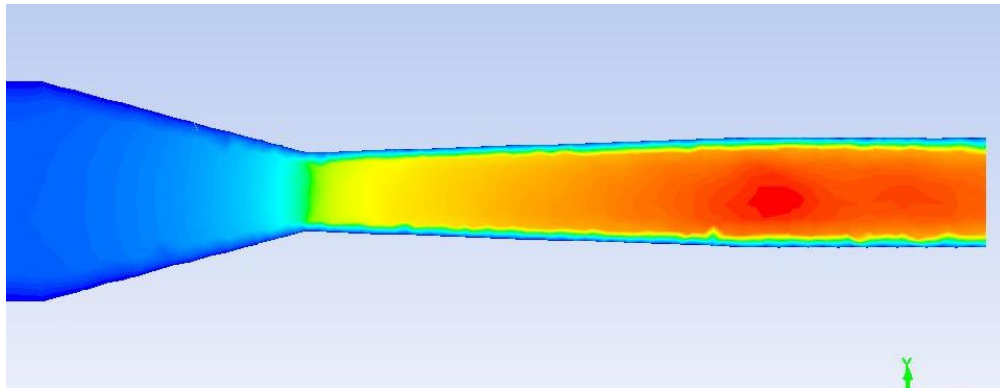


Figure 27: Converging-diverging nozzle boundary layer

3.2.5 Simplified Combustor Design

The velocity and temperature contours below reflect the low mixing efficiency of the simplified combustor model. The velocity peaked at 1820 m/s in the diverging section of the nozzle, then significantly decreased to about 1640 m/s in the barrel portion. Additionally, even though the temperature reached a satisfactory 3000K it was not uniform throughout. Figure 29 reveals a zone in the center of the nozzle where the temperature is as low as 2320K. This can be attributed to a high content of unburnt reactants.

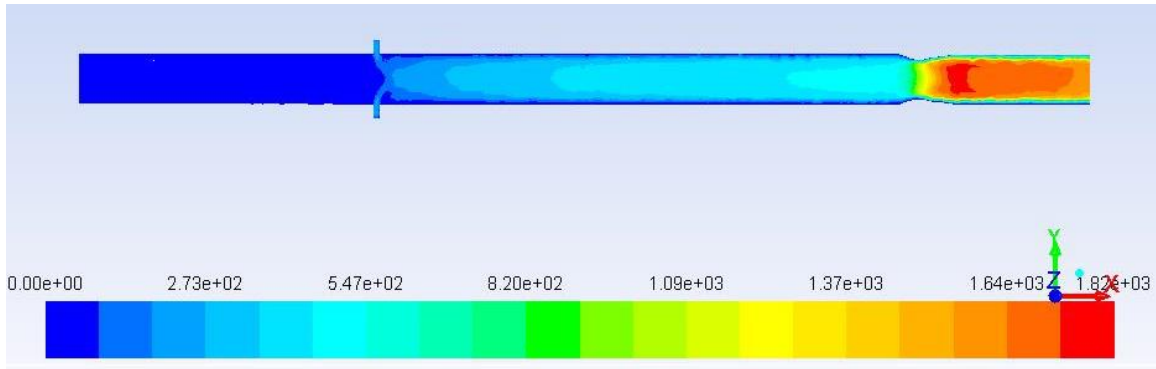


Figure 28: Simplified combustor velocity contour, units shown are in m/s

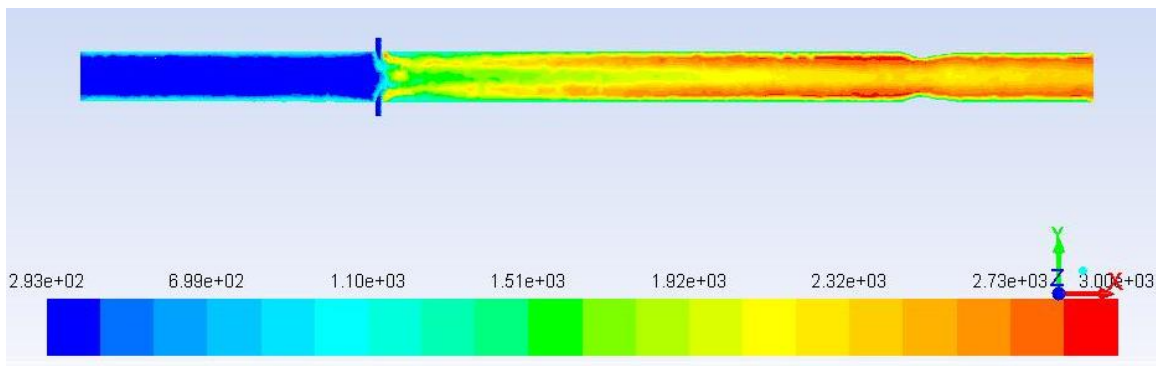


Figure 29: Simplified combustor temperature contour, units shown are in K

Contrary to the final design, the simplified combustor model lacked the orifice offset. The remaining variables such as combustion chamber diameter and injector dimensions remained constant. Figure 30 displays the methane vectors for such model. Four individual streams of fuel enter the combustion chamber in a cross manner but do not meet. The blue regions in the center and edges of the image are occupied by the oxygen being injected coaxially.

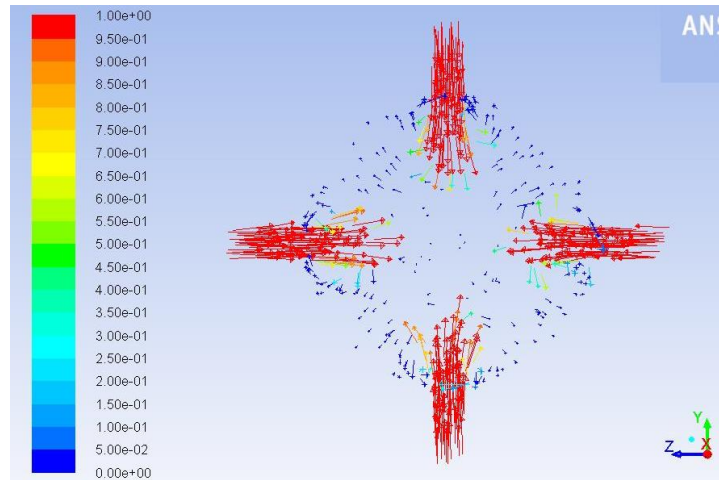


Figure 30: Simplified combustor methane velocity vectors

The methane and oxygen path-lines, shown in Figs. 31 and 32, aid to understand how the injector's geometry affects the mixing capabilities of the system. As the four jets of fuel are introduced into the combustion chamber they are quickly intercepted by the oxygen flow. It appears as if instead of mixing, the fuel is blown away by the oxidizer. Contrary to Fig. 26, the oxygen content does not seem to decrease significantly after the mixing point, meaning a high volume of unburnt oxygen.

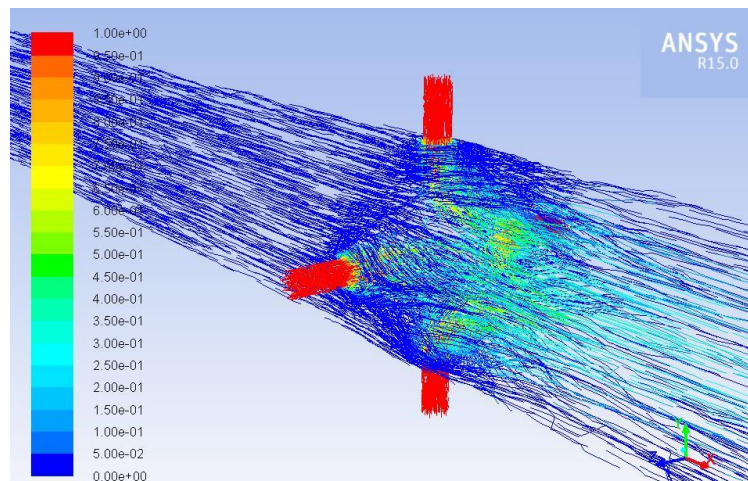


Figure 31: Simplified combustor methane pathlines

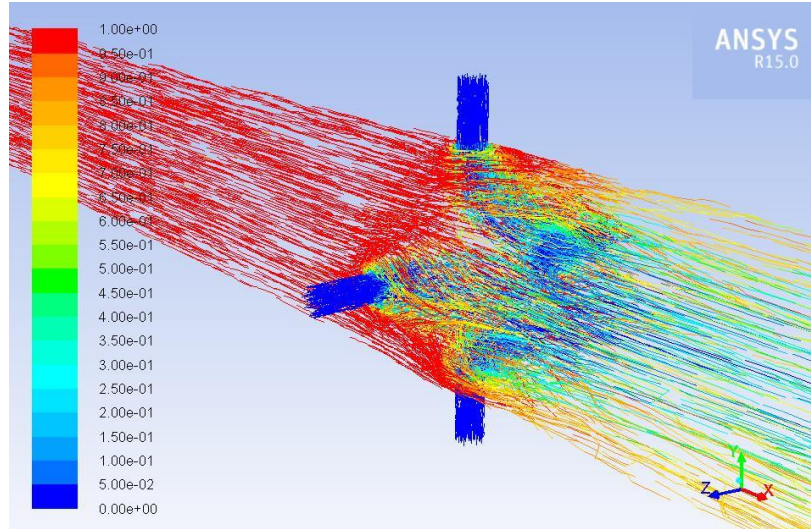


Figure 32: Simplified combustor oxygen pathlines

3.3 COOLING SYSTEM

3.3.1 Temperature

Using data from the combustion model the temperature contour for the coolant was obtained. It was determined that the highest temperature of 441K was reached at the water inlet. The highest temperature is observed at the water inlet because this area does not contain any channels that would increase the heat transfer rate. That region along with the nozzle experience the highest heat flux of 7.76 and 4.41MW/ m² respectively, causing the highest temperatures to be observed in both of these locations. The temperature remains near this value through the diverging section of the chamber. The temperature contour is presented in Fig. 33. As demonstrated in the image, the temperature begins to decrease upstream up to the injection point. This can be contributed to the lower heat flux encountered in the chamber region. The particular areas of interest were in the chamber where obstructions were placed for the static pressure and temperature measurement devices. These areas were of high interest because they would obstruct the flow of the water and decrease its velocity, providing the opportunity for hot spots and cavitation to occur within the channels. To ensure that cavitation would not be present, the maximum static pressure

and temperature in the channels was obtained. A static pressure of 856 kPa and temperature of 441K was calculated by Fluent. It is expected that cavitation will not occur since the saturation temperature of water at such pressure is 446K.

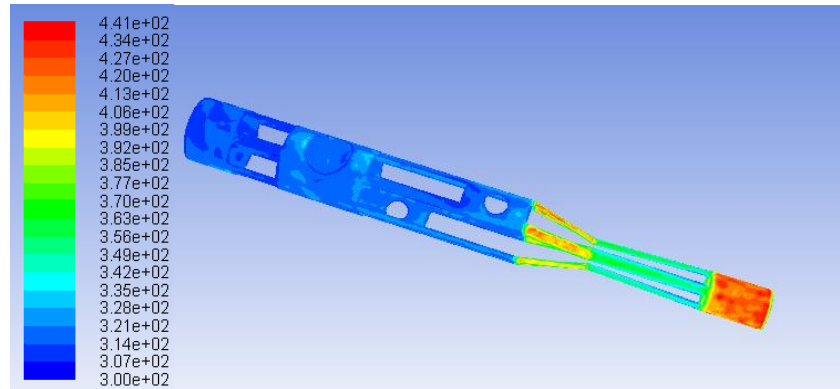


Figure 33: Temperature contour for the cooling system, units shown are in K

3.3.2 Simplified Cooling System Model

The pressure contour for the simplified cooling system model is shown in Fig. 34. The simulation which neglected any obstructions in the cooling channels computed a pressure drop of approximately 96.53 kPa, matching hand calculations. After validating that Fluent accurately models pressure differences a more complex model was developed. The new model (Fig. 33) revealed that the actual pressure drop was 551.58 kPa, almost 6 times larger than initially thought.

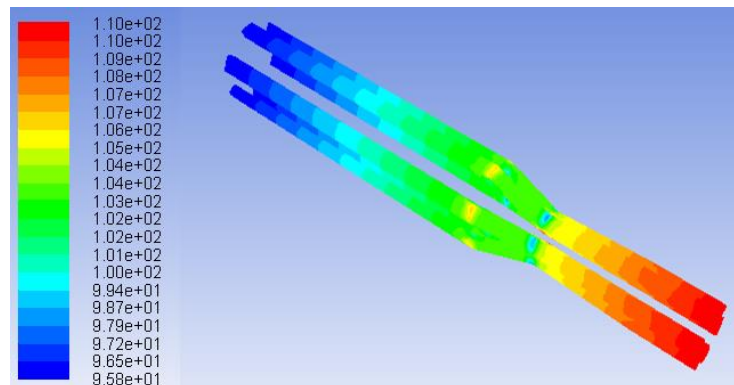


Figure 34: Simplified cooling system pressure contour

Chapter 4: Summary and Conclusions

Recent interest in efficient and low-pollution power generation has led to investigation of various energy producing devices. A technology that lost attractiveness among investors in the 20th century and now being revisited is magnetohydrodynamics (MHD). MHD power generators extract electrical energy directly from gases flowing through a magnetic field. Some advantages of these systems include:

- Higher efficiency due to the lack of mechanical components
- Potential to reach higher efficiencies than those of coal burning
- Higher thermal efficiencies associated with oxy-fuel combustion
- The system eliminates toxic combustion residuals making H₂O and CO₂ the only products, from which CO₂ can be sequestered
- MHD generators can be retrofitted into existing power plants, using the exhaust gases as energy source to generate steam

Some of the disadvantages are:

- Producing pure oxygen requires a lot of energy
- MHD generators are still in early stages and need more development

For this paper the modeling of various components of an MHD device are presented. This includes the fuel injector, combustor, nozzle, and cooling system. The main findings from this study are:

- In the fuel injector the counter-swirl inlets achieve a uniform pressure and velocity distribution when the L/D ratio is 4. Changes in the inlet location and orientation impacted pressure and velocity distribution. An angle of 115° in respect to the x-axis was found to increase distribution efficiency.
- Both the velocity and temperature criteria of 2000 m/s and 3000K ±10% were successfully achieved with the combustor. Data from NASA CEA and Fluent

matched within 4% and 9%, respectively. Differences may be attributed to CEA assumption of one-dimensional isentropic flow.

- A static pressure of 856 kPa and temperature of 441 K was calculated by Fluent. It is expected that cavitation will not occur since the saturation temperature of water at such pressure is 446K. It was also determined that the water flowed at an approximate volumetric flow rate of 17 LPM at an initial pressure of approximately 758.42 kPa. This will ensure that the cooling system will work effectively and the overall system will not fail.

While developing the various simulations it was always useful to start with a basic model and gradually add details making it more accurate. The simplicity of these models made it possible to validate Fluent's results by hand, proportioning confidence on the results of their more complex counterparts. They also permitted to freely explore different combinations of boundary conditions to find the ones that worked best.



Figure 35: DPE combustor

References

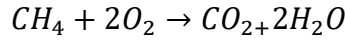
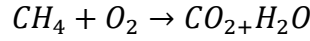
- ¹2013 EPA Reports retrieved from <https://www.epa.gov/climatechange/ghgemissions/usinventoryreport.html>
- ²Human Health and Environmental Effects of Emissions from Power Generation retrieved from <https://www.epa.gov/captrade/documents/power.pdf>
- ³Hunt, R., “The History of the Industrial Gas Turbine (Part 1 the first fifty years)”. *The Independent Technical Forum for Power Generation*, Vol. 582, 2011.
- ⁴Battery and Energy Technologies. (n.d.). Retrieved from https://www.mpoweruk.com/mhd_generator.html
- ⁵Richards, G. A. (2013, July). Future Combustion Technologies: Chemical Looping Combustion Direct Power Extraction Pressure gain combustion. Retrieved from [https://www.netl.doe.gov/File Library/events/2013/co2 capture/G-Richards-NETL-Future-Combustion.pdf](https://www.netl.doe.gov/File%20Library/events/2013/co2%20capture/G-Richards-NETL-Future-Combustion.pdf)
- ⁶Liu, BL, et al. "Three-Dimensional Analysis of the IEE MARK II MHD Generator". 9th International Conference on Magnetohydro-dynamic Electric Power Generation. Web.
- ⁷Malghan, V. , “History of MHD Power Plant Development” *Energy Conversion and Management*, Vol. 37, No. 5, May 1996, pp. 569-590.
- ⁸Anghaie, S., and Saraph, G., “Conceptual Design Analysis of An MHD Power Conversion System for Droplet-Vapor Core Reactors” Innovative Nuclear Space Power Institute DE-FG0593ER75871, 1995.
- ⁹Petrick M, Shumyatsky BYa, editors. Open-cycle magnetohydrodynamic electrical power generation. Technical and economic aspects of open-cycle MHD power plants, Nauka, Moscow and Argonne NL: Joint US–USSR Publication; 1978.
- ¹⁰Way, S., and Hundstad, R. , “Direct Generation of Power from a Combustion Gas Stream”, *Symposium (International) on Combustion*, Vol.8, No.1, 1991, pp.241-251.
- ¹¹Velikhov, E. P., Pismenny, V. D., Pisakin, A. V., Zhukov, B. B., and Sukharev, E. M. , “Pulsed MHD Power System SAKHALIN-The World Largest Solid Propellant Fueled MHD Generator of 500MWe Electric Power Output.” *Proceedings of 13th International Conference on MHD Power Generation and High Temperature Technologies*, Vol. 2, pp. 387-398. 1999
- ¹²Klepeis, James, and Vladimir Hruby. "MHD power generation experiments with a large disk channel-Verification of disk scaling laws." *Engineering Aspects of Magnetohydrodynamics*. Vol. 1. 1976
- ¹³Felderman, E. J., et. al., "HPDE Performance in the Faraday Mode", 20th EAMHD. Symposium, Irvine CA, June 1982, paper 4, 5.
- ¹⁴Aithal, S. , “Analysis of Optimum Power Extraction in a MHD Generator with Spatially Varying Electrical Conductivity, *International Journal of Thermal Sciences*, 2008, Vol.47, No.8, pp.1107-1112.
- ¹⁵Ishikwa, M., and Yuhara, M. , “Three-Dimensional Computation of Magnetohydrodynamics in Weakly Ionized Plasma with Strong MHD Interaction”, *Journal of Materials Processing Technology*, 2007, Vol. 181, No.1-3, pp. 254-259.
- ¹⁶Bhadoria, B., and Chandra, A. , “Transient Analysis of Proposed Indian MHD Channel” *Energy Conversion and Management*, 2001, Vol. 42, No.8, pp. 963-966.
- ¹⁷Wolfendale, M. , “A Coupled Systems Code-CFD MHD Solver for Fusion Blanket Design”, *Fusion Engineering and Design*, October 2015, Vol. 98-99, pp. 1902-1906

- ¹⁸Zubarov, V., and Egorychev, V. , “Design of Rocket for Spacecraft Using CFD- Modeling” *Scientific and Technological Experiments on Automatic Space Vehicles and Small Satellites*, Vol.104, pp. 29-35.
- ¹⁹Hernandez, M., Cabrera, L., Vidaña, O., Chaidez, M., Love, N., and Choudhuri, A., "Design of an Oxy-Methane Combustor for Direct Power Extraction," *AIAA-2016-0243*, 2016
- ²⁰Wendt, J. , *Governing Equations of Fluid Mechanics in Computational Fluid Dynamics an Introduction*, 3rd ed., Springer,Berlin, 2009.
- ²¹*Flow of fluids through valves, fittings, and pipe*. (1969). New York: Engineering Division Crane.
- ²²NASA Chemical Equilibrium with Applications (CEA). (n.d.). Retrieved from <http://www.grc.nasa.gov/WWW/CEAWeb>
- ²³Non-Premixed Combustion. (2013). In *ANSYS Fluent Theory Guide* (pp. 215-218).
- ²⁴Huang, D.H., and Huzel, D.K, *Modern Engineering for Design of Liquid Propellant Rocket Engines*, American Institute of Aeronautics and Astronautics, Washington D.C., 1992.
- ²⁵Betti, B., Nasuti, F., & Martelli, E. “Numerical simulation of hot-gas side heat transfer enhancement in thrust chambers by wall ribs” *AIAA Paper*, 5622, 2011.
- ²⁶Tu, J., & Yeoh, G., *Computational Fluid Dynamics a Practical Approach* 2nd ed., Butterworth-Heinemann, Waltham MA., 2008.
- ²⁷Boundary Layer. (n.d.). Retrieved from <https://www.grc.nasa.gov/www/k-12/airplane/boundlay.html>
- ²⁸Çengel, Y. A., & Cimbala, J. M. (2006). *Fluid mechanics: Fundamentals and applications*. Boston: McGraw-HillHigher Education.
- ²⁹Vidaña, O., Chaidez, M., Lovich, B., Aboud, J., Hernandez, M., Cabrera, L., Love, N., and Choudhuri, A., "Component and System Modeling of a Direct Power Extraction System," *AIAA-2016-0990*, 2016

Appendix A: Sample Calculations

FUEL & OXIDIZER MASS FLOW RATES

The first step was to balance the chemical reaction between Methane and Oxygen:



Oxygen and Methane have a molecular weight of 15.9994 and 16.04 g/mol, respectively. This means that 16.04 grams of methane react with 63.9976 grams of oxygen. Stoichiometric ratio is:

$$\frac{O}{F} = 3.99$$

However, it was decided for the DPE combustor to operate at a slightly rich equivalence ratio of 1.14. This yielded a mixture ratio of 3.49. Knowing this value allowed to develop a relationship between total and fuel mass flow rate.

$$\frac{\dot{m}_O}{\dot{m}_F} = 3.49$$

$$\dot{m}_T = \dot{m}_F + \dot{m}_O \rightarrow \dot{m}_T = \dot{m}_F(1 + 3.49) \rightarrow \frac{\dot{m}_T}{\dot{m}_F} = 4.49$$

CEA provided the velocity (1177.2 m/s) and density (0.35522 kg/m³) at the throat. Using that information and assuming a throat diameter of 3.68 mm total mass flow rate was computed:

$$\dot{m}_T = \rho AV = \mathbf{0.004496 \text{ kg/s}}$$

It was then possible to calculate the methane and oxygen individual flow rates:

$$\dot{m}_F = \frac{\dot{m}_T}{4.49} = \mathbf{0.001001 \text{ kg/s}}$$

$$\dot{m}_O = 3.49 * \dot{m}_F = \mathbf{0.003495 \text{ kg/s}}$$

Table 11: Flow rate calculation variables

| Symbol | Name | Units |
|-------------|------------------------|----------|
| A | Area | m^2 |
| ρ | Density | kg/m^3 |
| \dot{m}_F | Methane mass flow rate | kg/s |
| \dot{m}_O | Oxygen mass flow rate | kg/s |
| \dot{m}_T | Total mass flow rate | kg/s |
| V | Velocity | m/s |

THROAT CONDITIONS

The first step while calculating the throat's local heat flux was using Bartz Correlation to find the heat transfer coefficient²⁴:

$$h_g = \left[\frac{0.026}{D_t^{0.2}} \left(\frac{\mu^{0.2} c_p}{Pr^{0.6}} \right) \left(\frac{(p_c)g}{c^*} \right) \left(\frac{Dt}{R} \right)^{0.1} \right] \times \frac{A_t^{0.9}}{A} \sigma$$

Some variables such as D_t , R , A_t , A were directly dependent on the combustor's geometry. The rest of the values were retrieved from CEA after making the following set of assumptions; equivalence ratio of 1.14, chamber pressure of 758.42 kPa and expansion ratio of 1.85.

In order to calculate σ the following formula was employed²⁴:

$$\sigma = \frac{1}{\left[\frac{1}{2} \frac{T_{wg}}{T_c} \left(1 + \frac{\gamma-1}{2} M^2 \right) + \frac{1}{2} \right]^{0.68} \left[1 + \frac{\gamma-1}{2} M^2 \right]^{0.12}}$$

T_{wg} was set to 525 °C due to Inconel 718's thermal properties, and M to 1 since the point of interest was the throat. The remaining values were acquired from CEA. This yielded an h_g of 4544 W/m²-K. However, as previously explained Bartz correlation tends to overestimate the convective heat transfer coefficient, for which it was reduced by 40%.

$$h_g \times 0.6 = \mathbf{2726 \text{ W/m}^2\text{K}}$$

Once h_g was corrected, the heat flux could be calculated²⁴:

$$q = h_g (T_{aw} - T_{wg}) = \mathbf{6.86 \text{ MW/m}^2}$$

Table 12: Heat flux calculation values

| Symbol | Name | Value | Units |
|----------|--------------------------------------|---------|------------------|
| T_{aw} | Adiabatic wall temperature | 3146.27 | K |
| c^* | Characteristic velocity | 1813.6 | m/s |
| A | Combustion chamber area | 78.54 | mm ² |
| T_c | Combustion chamber temperature | 3178.05 | K |
| μ | Dynamic viscosity | 1.043 | kg/m-s |
| g | Gravity | 9.81 | m/s ² |
| M | Mach number | 1 | N/A |
| Pr | Prandtl number | 0.67 | N/A |
| R | Radius of inner shell | 2.76 | mm |
| c_p | Specific heat | 2.28 | kJ/kg-K |
| γ | Specific heat ratio | 1.12 | N/A |
| T_{wg} | Temperature of the hot-gas-side wall | 525 | °C |
| A_t | Throat area | 10.64 | mm ² |
| D_t | Throat diameter | 3.68 | mm |

Moreover, knowing the heat flux made it possible to obtain the combustor's wall (static and thermal) combined stress using²⁴:

$$S_c = \frac{(p_{co} - p_g)R}{t} + \frac{Eaqt}{2(1 - \nu)k} = \mathbf{610 \text{ MPa}}$$

Inconel 718 has a coefficient of thermal expansion of 7.8×10^{-6} , a Poisson's ratio of 0.275, and a modulus of elasticity of 170.3 GPa at ~525 °C. The value of t was varied attempting to find the optimal thickness. After analyzing how the wall thickness impacts the combustor's structural integrity, it was decided to constrain it at 1 mm.

Table 13: Combined stress calculation values

| Symbol | Name | Value | Units |
|----------|----------------------------------|----------------------|-------|
| a | Coefficient of thermal expansion | 7.8×10^{-6} | N/A |
| p_g | Combustion-gas pressure | 758.42 | kPa |
| p_{co} | Coolant pressure | 1034.21 | kPa |
| E | Modulus of elasticity | 170.3 | GPa |
| ν | Poisson's ratio | 0.275 | N/A |
| R | Radius of inner shell | 2.76 | mm |
| k | Thermal conductivity | 11.4 | W/m-K |
| t | Wall thickness | 1 | mm |

COOLING SYSTEM PUMP OPTIMAL FLOW RATE

While finding the pump's ideal operating condition GPM, feet, and psi were employed as those are the units listed in the pump's specification sheet. It was previously determined that an adequate water flowrate required to effectively cool down the combustor was 4.23 GPM (16 LMP). In order to calculate the pressure drop induced by some of the cooling system's components the following equation was implemented²¹:

$$C_v = \frac{V}{\sqrt{\frac{\Delta P}{SG}}}$$

Where C_v stands for valve flow coefficient, V for flow rate, ΔP for pressure drop, and SG for specific gravity.

Table 14: Componets pressure drop

| Component | Flow Rate (GPM) | SG | Cv | Quantity | ΔP (psi) |
|------------------|-----------------|----|------|----------|------------------|
| Ball valve | 4.23 | 1 | 12 | 2 | 0.25 |
| Small ball valve | 4.23 | 1 | 4.4 | 4 | 3.69 |
| Needle valve | 4.23 | 1 | 0.73 | 1 | 33.52 |

The loss coefficient for sudden expansions was estimated with equation²⁸:

$$K_L = \left(1 - \frac{d^2}{D^2}\right)^2$$

Furthermore, Fig. 36²⁸ was employed to calculate the loss coefficient caused by the sudden contractions. Where K_L stands for loss coefficient, d for small diameter, and D for large diameter.

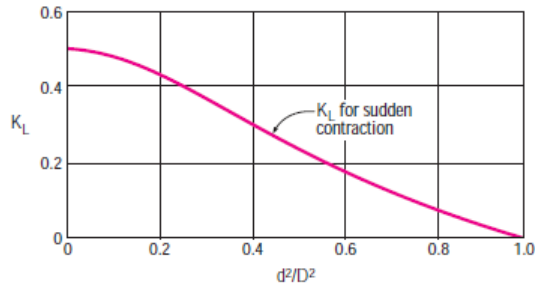


Figure 36: Sudden contractions loss coefficient chart

Next, the head loss was calculated using equation²⁸:

$$h_L = K_L \frac{V^2}{2g}$$

Where h_L stands for head loss, V for velocity, and g for gravity.

With that information it was possible to obtain the pressure drop using relationship²⁸:

$$\Delta P = \rho g h_L$$

The same process was followed to approximate the pressure drop caused by the multiple bends.

Table 15: Sudden expansion, sudden contraction and bends pressure drop

| Type | d (ft.) | D (ft.) | K_L | Velocity (ft/s) | h_L (ft) | Quantity | ΔP (psi) |
|------------------------|---------|---------|-------|-----------------|------------|----------|------------------|
| Sudden expansion | 0.0125 | 0.029 | 0.63 | 33.73 | 6.66 | 1 | 4.79 |
| Sudden contraction | 0.0125 | 0.029 | 0.42 | 33.73 | 0.3 | 1 | 3.22 |
| Sudden contraction (2) | 0.029 | 0.083 | 0.46 | 14.11 | 0.43 | 1 | 0.62 |
| 90° bends | N/A | N/A | 0.3 | 14.11 | 0.23 | 15 | 6.02 |
| 180° bends | N/A | N/A | 0.2 | 7.05 | 0.05 | 2 | 0.13 |

Major losses were computed implementing Darcy's equation²⁸:

$$\Delta P = f \frac{L}{D} \frac{\rho V^2}{2} = 33.77 \text{ psi}$$

Where f stands for friction factor, L for pipe length, D for hydraulic diameter, and ρ for density. The flow resulted to be turbulent, for which the friction factor was acquired by means of the Moody Chart.

Table 16: Pressure drop along the pipes

| Diameter (ft.) | Velocity (ft/s) | Friction factor | Length (ft.) | ΔP (psi) |
|----------------|-----------------|-----------------|--------------|------------------|
| 0.029 | 14.11 | 0.024 | 28 | 29.43 |
| 0.0125 | 33.73 | 0.023 | 0.25 | 4.34 |

The test article's pressure drop was also taken into account, according to Fluent it was approximately 80 psi. Once the total pressure drop was obtained (148 psi), it was translated into total head loss. Then it was converted again into a loss coefficient to have a unit-less term²⁸:

$$h_L = \frac{\Delta P}{\rho g} = 341.31 \text{ ft.} \quad K_L = \frac{h_L}{\left(\frac{V^2}{2g}\right)} = 110.59$$

Holding the value of the combined loss coefficient allowed to plot the system curve at different flow rates (Table 17). Comparing it side to side with the Pump Performance Curve provided by the manufacturer yielded the optimal flow rate for the system, **5 GPM (~19 LPM)** (Fig. 37). This means that more than enough coolant will be supplied to the system, while a proportional control valve enables flow adjustment. The water line schematic is provided in Appendix B.

Table 17: Head loss and ΔP at various flow rates

| GPM | KL | hL (ft.) | ΔP (psi) |
|------------|-----------|-----------------|------------------------------------|
| 0 | 110.59 | 0 | 0 |
| 1 | 110.59 | 19.10 | 8.29 |
| 2 | 110.59 | 76.42 | 33.14 |
| 4 | 110.59 | 305.67 | 132.56 |
| 6 | 110.59 | 687.76 | 298.27 |
| 8 | 110.59 | 1222.7 | 530.25 |
| 10 | 110.59 | 1910.45 | 828.52 |
| 12 | 110.59 | 2751.05 | 1193.07 |
| 14 | 110.59 | 3744.49 | 1623.9 |
| 16 | 110.59 | 4890.76 | 2121.01 |
| 18 | 110.59 | 6189.86 | 2684.4 |
| 20 | 110.59 | 7641.81 | 3314.07 |

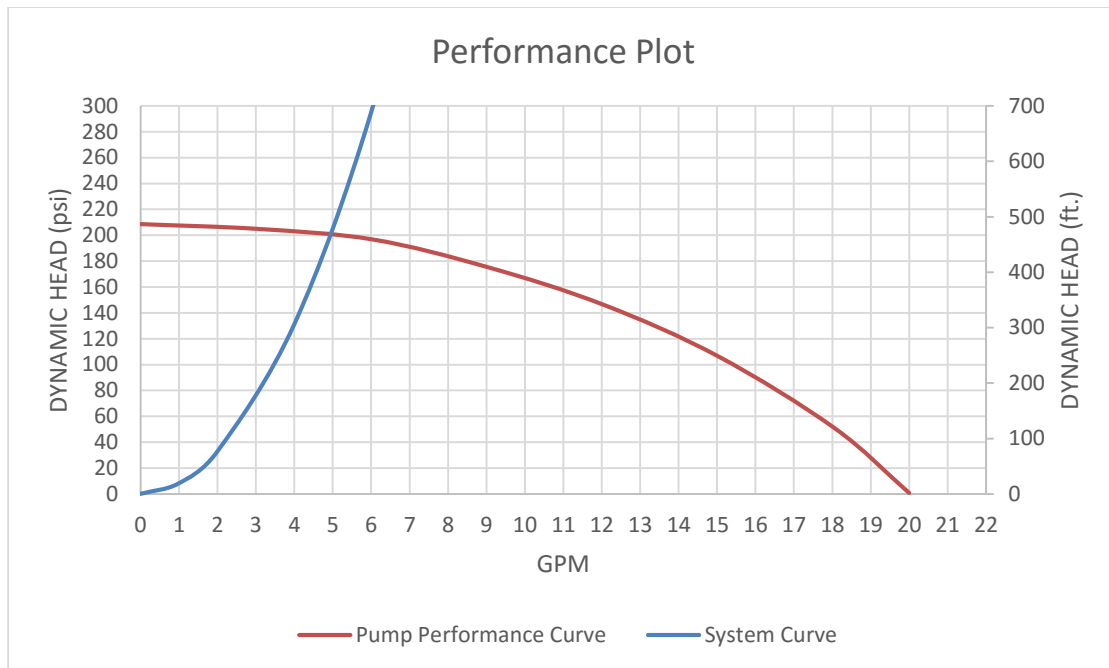


Figure 37: Pump performance curve vs. System curve

CEA RESULTS

NASA-GLENN CHEMICAL EQUILIBRIUM PROGRAM CEA2, MAY 21, 2004
 BY BONNIE MCBRIDE AND SANFORD GORDON
 REFS: NASA RP-1311, PART I, 1994 AND NASA RP-1311, PART II, 1996

```
problem  phi,eq.ratio=1.14,
          rocket equilibrium
          p,psia=110,
          sup,ae/at=1.85,
react
  fuel=CH4 moles=1  t,k=298
  oxid=O2 moles=1  t,k=298
output  short transport
end
```

THEORETICAL ROCKET PERFORMANCE ASSUMING EQUILIBRIUM

COMPOSITION DURING EXPANSION FROM INFINITE AREA COMBUSTOR

Pin = 110.0 PSIA
 CASE =

| | REACTANT | MOLES | ENERGY KJ/KG-MOL | TEMP K |
|---------|----------|-----------|---------------------|-----------|
| FUEL | CH4 | 1.0000000 | -74605.353 | 298.000 |
| OXIDANT | O2 | 1.0000000 | -4.407 | 298.000 |

O/F= 3.49935 %FUEL= 22.225413 R,EQ.RATIO= 1.140000 PHI,EQ.RATIO= 1.140000

| | CHAMBER | THROAT | EXIT |
|-----------------|----------|----------|----------|
| Pinf/P | 1.0000 | 1.7203 | 6.5619 |
| P, BAR | 7.5842 | 4.4086 | 1.1558 |
| T, K | 3315.90 | 3178.05 | 2873.78 |
| RHO, KG/CU M | 5.7697-1 | 3.5522-1 | 1.0666-1 |
| H, KJ/KG | -1033.70 | -1726.63 | -3279.33 |
| U, KJ/KG | -2348.19 | -2967.70 | -4362.95 |
| G, KJ/KG | -44444.3 | -43332.6 | -40901.8 |
| S, KJ/(KG) (K) | 13.0916 | 13.0916 | 13.0916 |
| M, (1/n) | 20.974 | 21.291 | 22.050 |
| (dLV/dLP)t | -1.05703 | -1.05250 | -1.04108 |
| (dLV/dLT)p | 2.0724 | 2.0328 | 1.8993 |
| Cp, KJ/(KG) (K) | 10.3507 | 10.2799 | 9.7398 |
| GAMMAS | 1.1204 | 1.1167 | 1.1094 |
| SON VEL,M/SEC | 1213.6 | 1177.2 | 1096.4 |
| MACH NUMBER | 0.000 | 1.000 | 1.933 |

TRANSPORT PROPERTIES (GASES ONLY)
 CONDUCTIVITY IN UNITS OF MILLIWATTS/(CM) (K)

VISC,MILLIPOISE 1.0720 1.0430 0.97877

WITH EQUILIBRIUM REACTIONS

Cp, KJ/(KG) (K) 10.3507 10.2799 9.7398
 CONDUCTIVITY 22.9221 21.9001 18.8055
 PRANDTL NUMBER 0.4841 0.4896 0.5069

WITH FROZEN REACTIONS

Cp, KJ/(KG) (K) 2.2868 2.2766 2.2507
 CONDUCTIVITY 3.6880 3.5403 3.2151
 PRANDTL NUMBER 0.6647 0.6707 0.6852

PERFORMANCE PARAMETERS

Ae/At 1.0000 1.8500
 CSTAR, M/SEC 1813.6 1813.6
 CF 0.6491 1.1685
 Ivac, M/SEC 2231.5 2630.6
 Isp, M/SEC 1177.2 2119.3

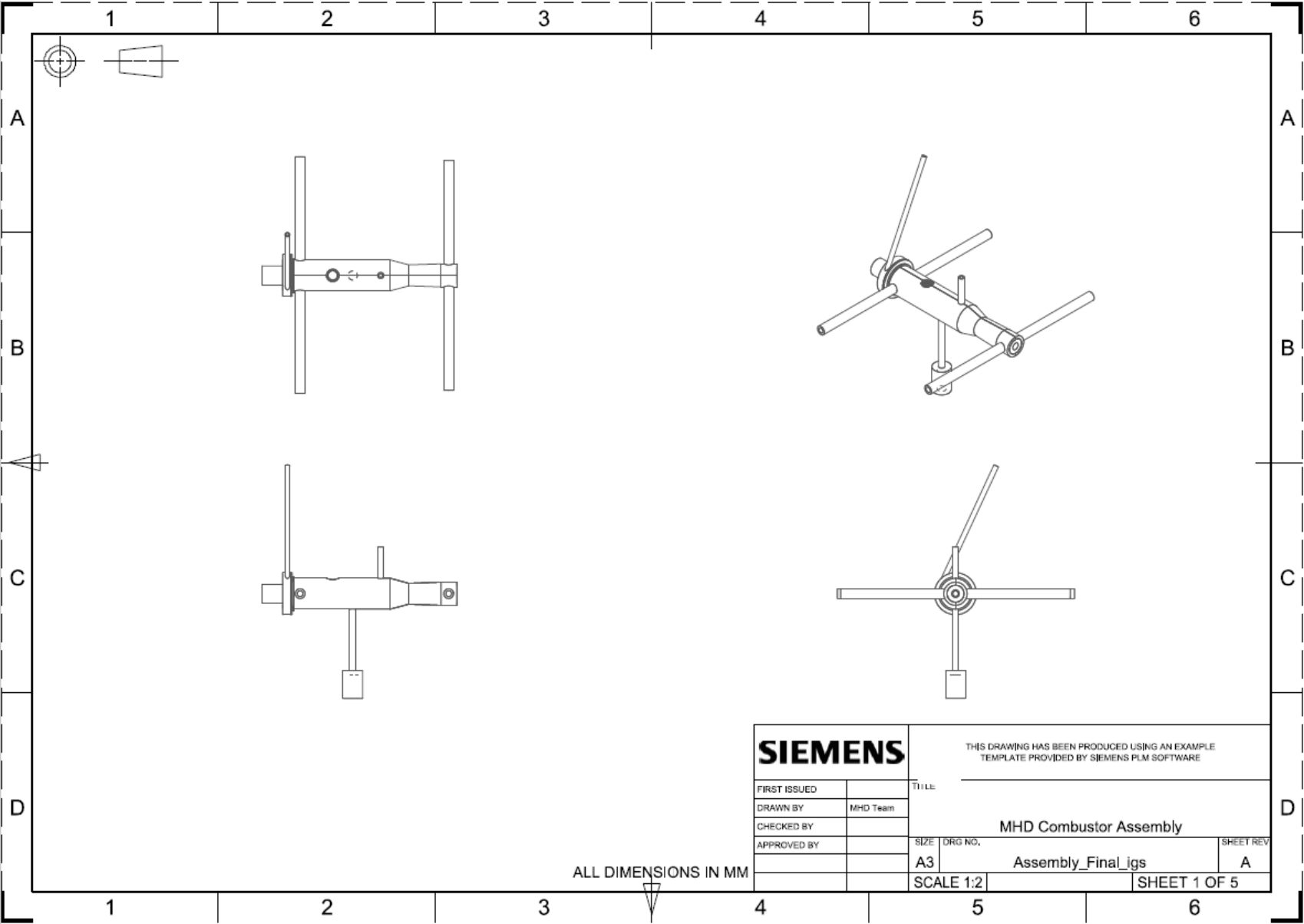
MOLE FRACTIONS

*CO 0.18178 0.17614 0.16019
 *CO2 0.10879 0.11883 0.14529
 *H 0.04134 0.03691 0.02710
 HO2 0.00007 0.00005 0.00002
 *H2 0.08934 0.08547 0.07617
 H2O 0.42718 0.44668 0.49268
 H2O2 0.00001 0.00000 0.00000
 *O 0.02229 0.01882 0.01157
 *OH 0.08783 0.07862 0.05713
 *O2 0.04137 0.03848 0.02984

* THERMODYNAMIC PROPERTIES FITTED TO 20000.K

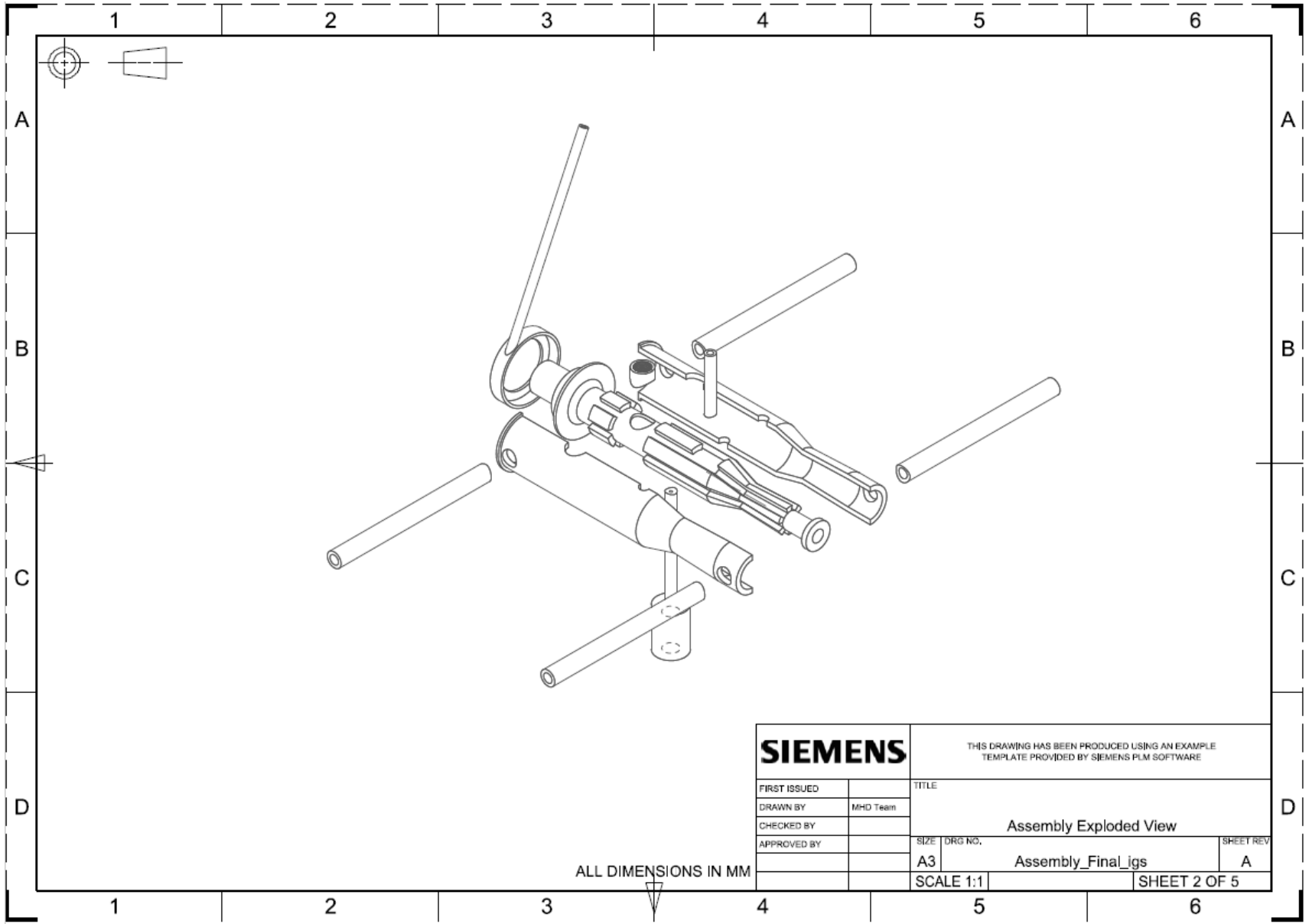
Appendix B: CADs and Schematics

DPE COMBUSTOR ASSEMBLY

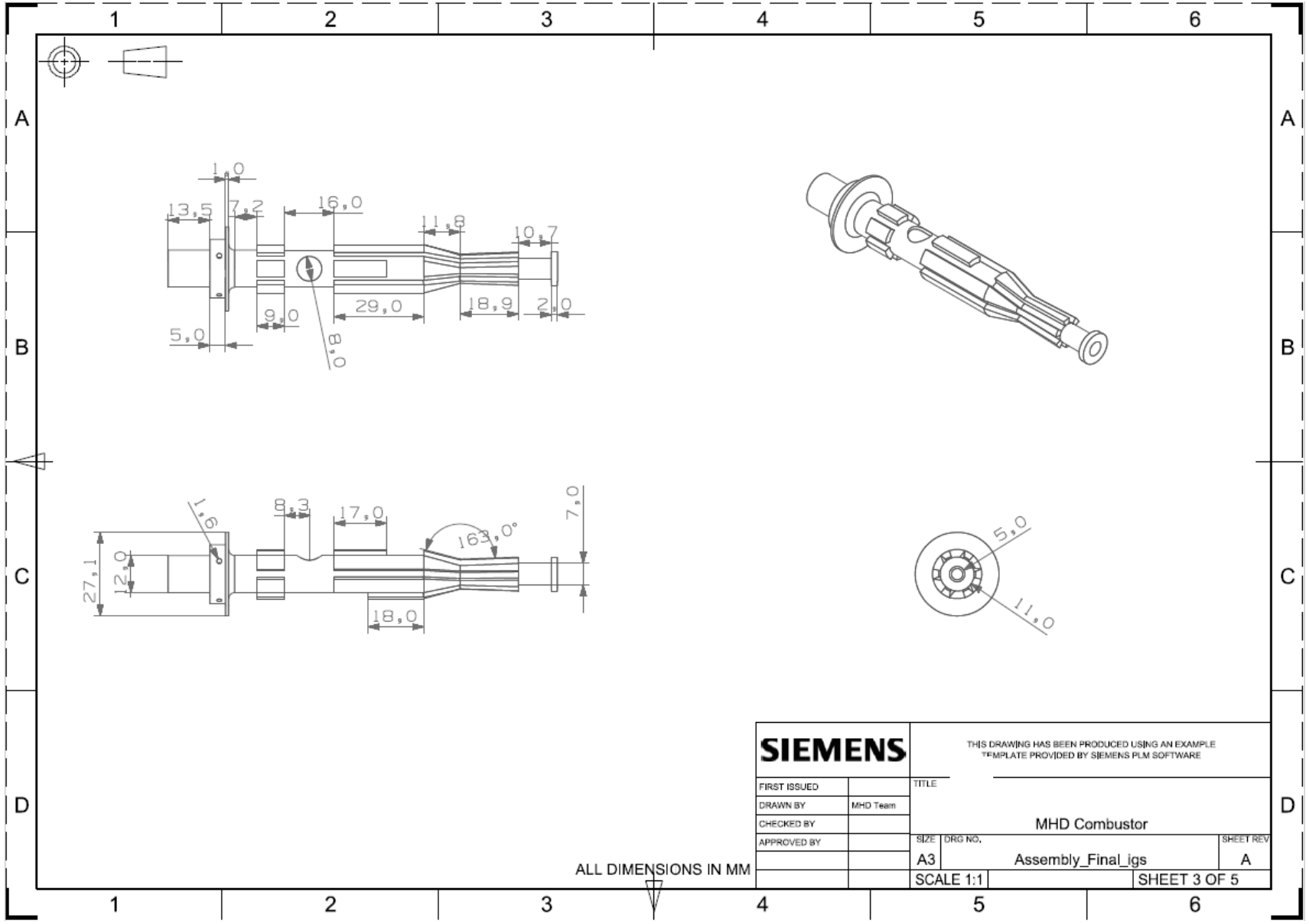


D

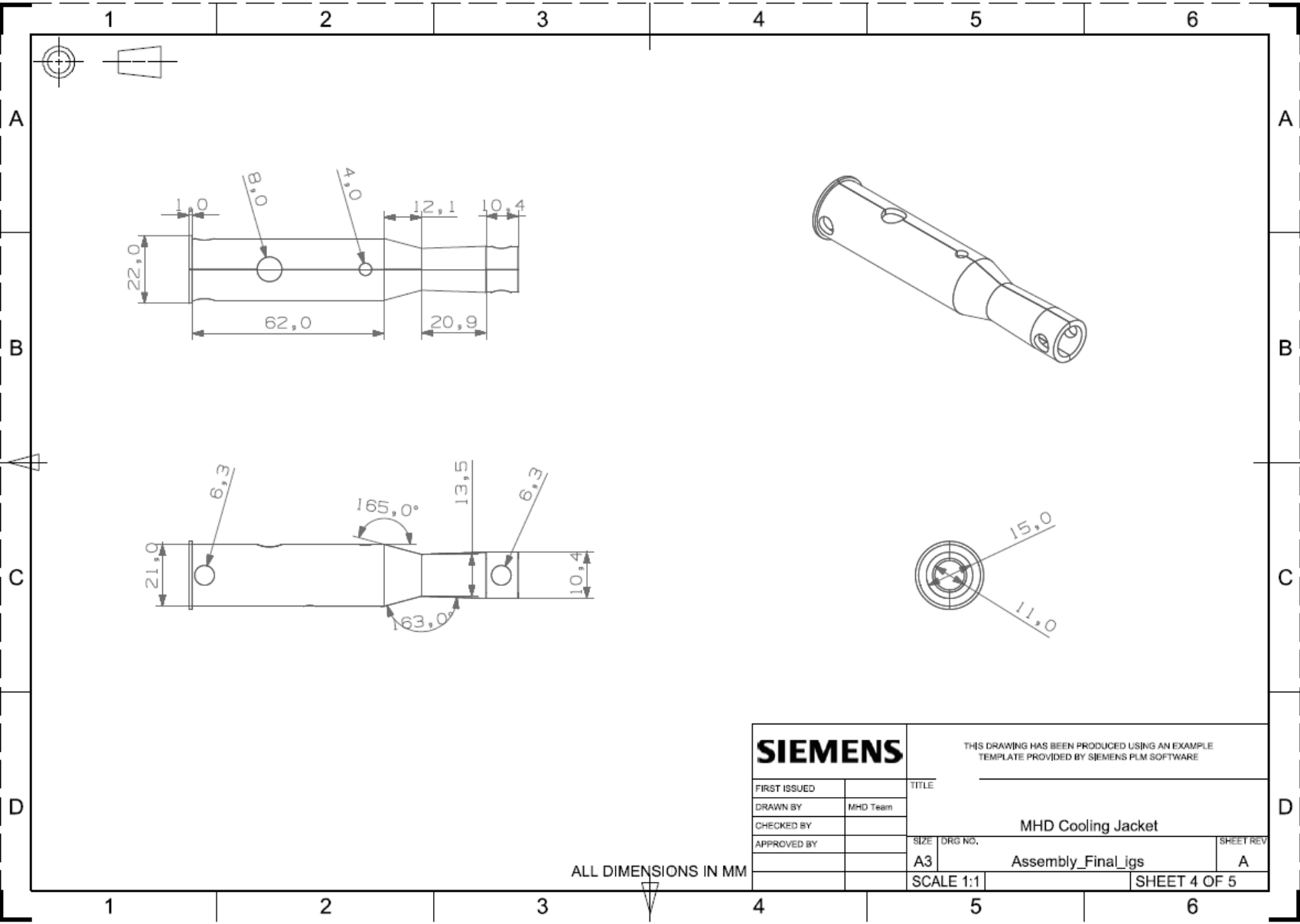
DPE COMBUSTOR EXPLODED VIEW



DPE COMBUSTOR

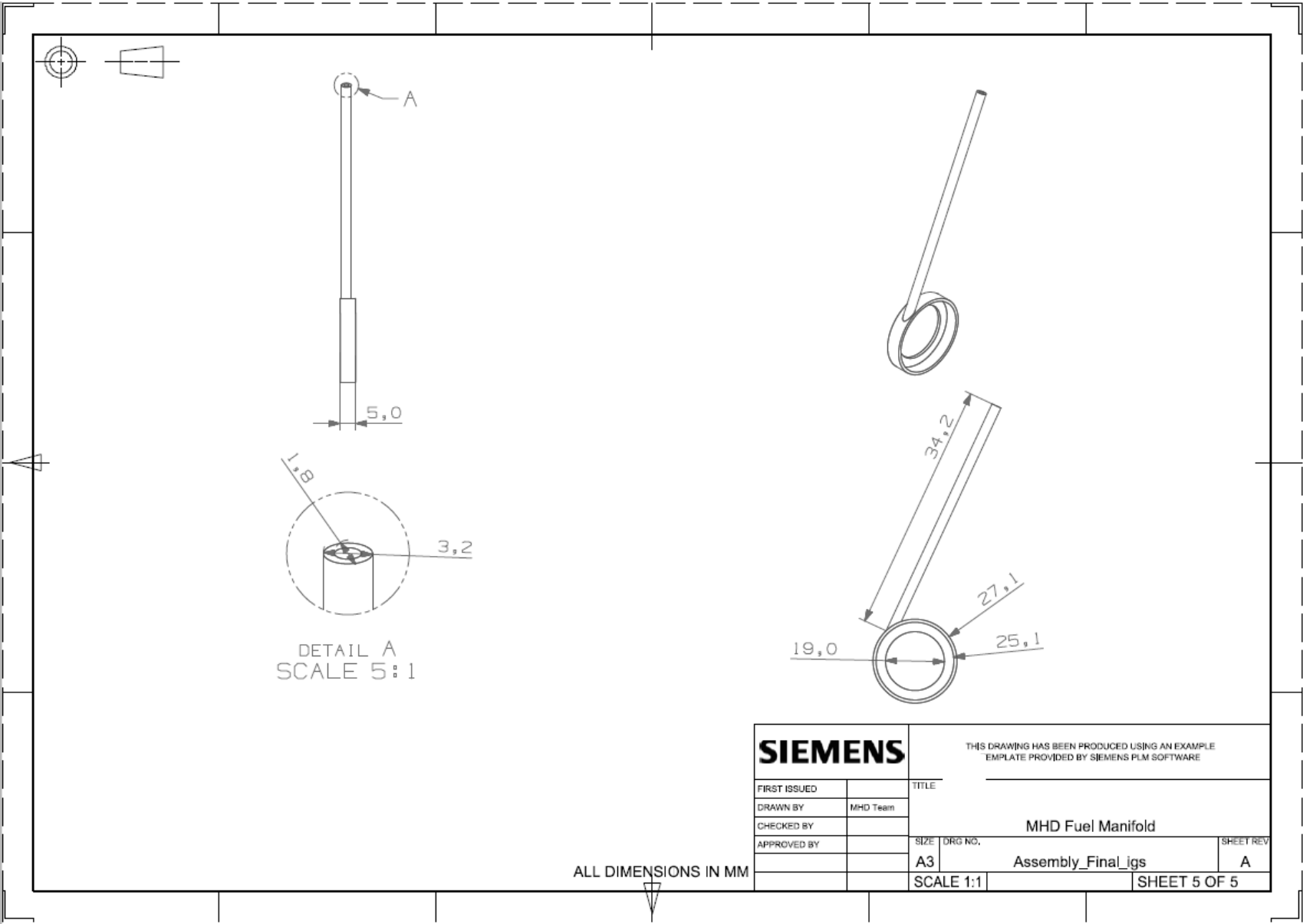


COOLING JACKET

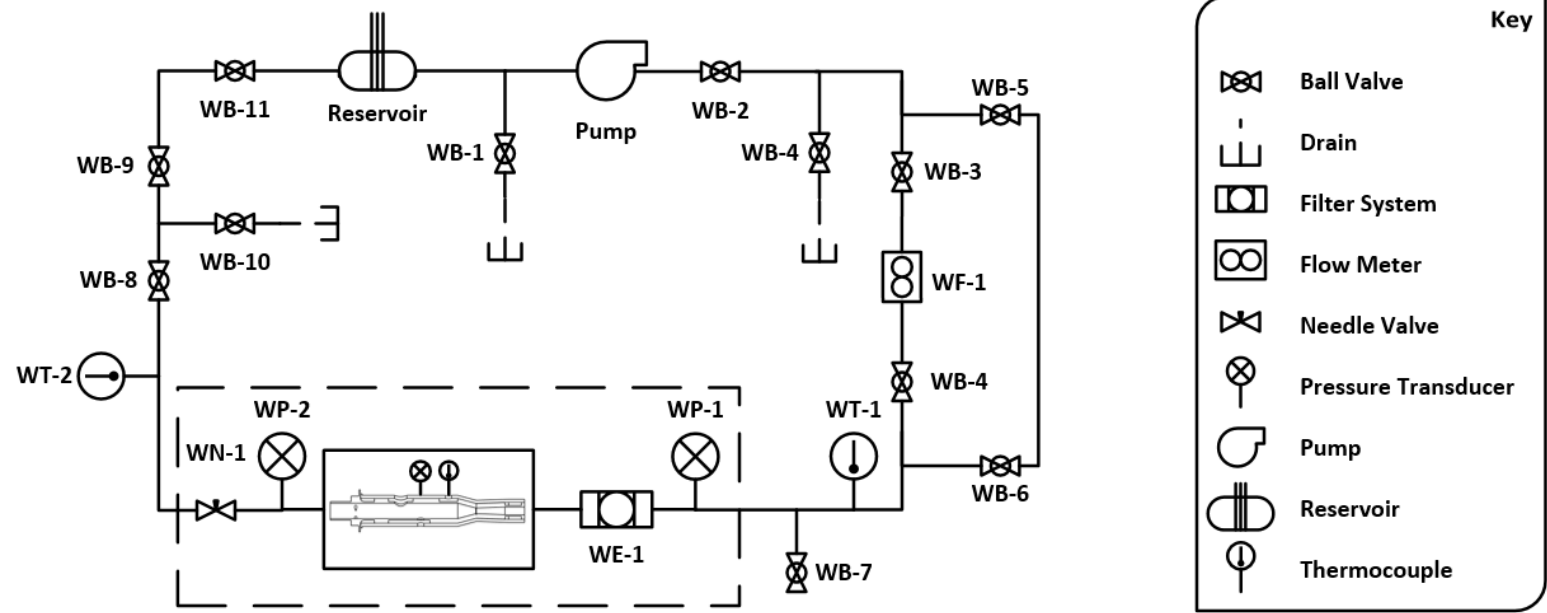


| | | | |
|----------------|----------|--|--------------------|
| SIEMENS | | THIS DRAWING HAS BEEN PRODUCED USING AN EXAMPLE TEMPLATE PROVIDED BY SIEMENS PLM SOFTWARE | |
| FIRST ISSUED | | TITLE | |
| DRAWN BY | MHD Team | MHD Cooling Jacket | |
| CHECKED BY | | SIZE | DRG NO. |
| APPROVED BY | | A3 | Assembly_Final_igs |
| | | SCALE 1:1 | SHEET 4 OF 5 |

FUEL MANIFOLD



WATER LINE SCHEMATIC



Vita

Omar D. Vidaña was born in El Paso, Texas, on May 14, 1990. Shortly after that, his family moved to Zacatecas, Mexico where he lived until he was 10 years old. Following high-school graduation, he joined the University of Texas at El Paso to pursue a career in Mechanical Engineering. After earning his Bachelor's degree in May of 2014, he decided to continue his education by enrolling a graduate program at the same institution. A few months later, he was employed as a Research Assistant at the Center for Space Exploration Technology Research Lab under Dr. Norman Love. There he was teamed with a group of graduate students to develop and supersonic, liquid-cooled combustor, intended to be used in a direct power extraction system. His work during the project resulted in three publications, one of them was awarded best paper by the AIAA Terrestrial Committee at the 2016 SciTech Conference in San Diego, California. On August, 2016 he was given the title of Master of Science in Mechanical Engineering.

Permanent address: 5465 Gate Ridge Cir.

El Paso, Texas, 79932

This thesis was typed by Omar D. Vidaña